HAL
open science

Curvature gradient drives polarized tissue flow in the Drosophila embryo

Emily Gehrels, Bandan Chakrabortty, Matthias Merkel, Thomas Lecuit

To cite this version:

Emily Gehrels, Bandan Chakrabortty, Matthias Merkel, Thomas Lecuit. Curvature gradient drives polarized tissue flow in the Drosophila embryo. 2022. hal-03796461

HAL Id: hal-03796461

https://hal.science/hal-03796461v1

Preprint submitted on 4 Oct 2022

HAL is a multi-disciplinary open access archive for the deposit and dissemination of scientific research documents, whether they are published or not. The documents may come from teaching and research institutions in France or abroad, or from public or private research centers.

L'archive ouverte pluridisciplinaire **HAL**, est destinée au dépôt et à la diffusion de documents scientifiques de niveau recherche, publiés ou non, émanant des établissements d'enseignement et de recherche français ou étrangers, des laboratoires publics ou privés.

PNAS

Main Manuscript for

Curvature gradient drives polarized tissue flow in the *Drosophila* embryo.

Emily Gehrels[1,†], Bandan Chakrabortty[1,†], Matthias Merkel[2,*] & Thomas Lecuit[1,3,*]

[1] IBDM - UMR7288 & Turing Centre for Living Systems, Aix Marseille Université & CNRS, Marseille, France 13288

[2] Centre de Physique Theorique - UMR7332 & Turing Centre for Living Systems, Aix Marseille Université & CNRS, Marseille, France 13288

[3] Collège de France, Paris, France 75005

†, * These authors contributed equally to this work

* Corresponding authors: Matthias Merkel and Thomas Lecuit

Emails: matthias.merkel@univ-amu.fr; thomas.lecuit@univ-amu.fr

Author Contributions: E.W.G., B.C., M.M. and T.L. conceived the project. E.W.G. and T.L. planned the experiments. E.W.G. performed the experiments. B.C. and M.M. developed the model. B.C. wrote all code used, and performed simulations and data fitting. E.W.G. and B.C. performed all data analysis. E.W.G., B.C., M.M. and T.L. discussed the data and wrote the manuscript.

Competing Interest Statement: The authors declare no competing interests.

Preprint Servers: This manuscript has been deposited as a preprint on the bioRxiv.

Classification: Biological Sciences (Developmental Biology) and Physics (Biophysics and Computational Biology)

Keywords: Morphogenesis, *Drosophila*, geometry, myosin-driven contractility, mechanics

This PDF includes:

Main Text
Figures 1 to 6

Abstract

Tissue flow during morphogenesis is commonly driven by local constriction of cell cortices, which is caused by activation of actomyosin contractility. This can lead to long-range flows due to tissue viscosity. However, in the absence of cell-intrinsic polarized forces or polarity in forces external to the tissue, these flows must be symmetric and centered around the region of contraction. Polarized tissue flows have been previously demonstrated to arise from the coupling of such contractile flows to points of increased friction or adhesion to external structures. However, we show with experiments and modeling that the onset of polarized tissue flow in early *Drosophila* morphogenesis occurs independent of adhesion and is instead driven by a geometric coupling of apical actomyosin contractility to tissue curvature. Particularly, the onset of polarized flow is driven by a mismatch between the position of apical myosin activation and the position of peak curvature at the posterior pole of the embryo. Our work demonstrates how genetic and geometric information inherited from the mother interact to create polarized flow during embryo morphogenesis.

Significance Statement

Much is known about how genetic prepatterning of the embryo defines initial instructions for morphogenesis, but how these instructions are deployed in a specific mechanical and geometrical environment is unknown. In our manuscript, we use *Drosophila* embryos to explore how genetics, mechanics, and geometry interact to drive polarized (directional) tissue flow. Through a combination of experimental and modeling approaches, we show that previously proposed mechanisms cannot account for the tissue flows observed during the early stages of *Drosophila* morphogenesis. Instead, we reveal a novel mechanism whereby polarized flows arise from the interaction between myosin-driven tissue contraction and the curvature of the tissue imposed by the shape of the egg.

Main Text

Introduction

Morphogenesis is the process by which organisms develop from a simple fertilized egg to an adult with complex form and function. This process depends keenly on the dynamics of the underlying biological tissues, which itself arises from cellular attributes such as cell-cell adhesion, cortical tension, osmotic

pressure, elasticity, and viscosity, all of which can be passively and actively controlled in space and time (1, 2). Tissue-scale effects can arise as a result of local changes to these cellular attributes. For example, tissue invagination emerges from apical constriction of well-defined groups of cells (3) such as in the mesoderm or endoderm of *C. elegans* (4, 5), *Drosophila* (6), sea urchin (7), or ascidians (8, 9).

Tissue flows are ubiquitous in animal development, especially during embryogenesis and organogenesis. Tissue flow may be symmetric or polarized (asymmetric and vectorial) depending on the pattern and polarity of internal active stresses and on the existence of external polarized active stress acting on the tissue (2). When no external polarized force exists, flow is intrinsically symmetric. Cells may converge towards a group of constricting cells such as on either side of the *Drosophila* mesoderm (10). Alternatively, anisotropic forces driving cell division can give rise to local divergent flow due to bipolar cell displacement (11, 12) or tissue extension (13). These two types of symmetric flows may coexist, perpendicular to each other, during the process of so-called convergent extension. During this process, cell intercalation causes local divergent flow and perpendicular convergence due to junction shrinkage along one axis, and junction extension along the perpendicular axis (14–21). In contrast, the emergence of polarized flow depends upon the presence of an external acting force. For instance, contraction of the hinge at the proximal end of the developing *Drosophila* pupal wing and anchoring of the wing at its distal tip drive polarized tissue flow and global extension of the wing (12, 22, 23). Similarly, a supracellular tensile ring in the posterior of chick epiblast drives non-local polarized rotational flows in the whole embryonic field during primitive streak formation (24).

During early *Drosophila* morphogenesis, a single layer of epithelial cells is formed by the simultaneous cellularization of the 6000 nuclei composing the syncytial blastoderm (25). Subsequently, at the onset of gastrulation, this initially static tissue begins to flow and thereby initiates the process of axis elongation along the antero-posterior axis (14, 15). Most notably, the tissue in the posterior of the embryo, called the endoderm, undergoes a polarized flow towards the dorsal-anterior side of the embryo (16, 26) (**Movie S1**, **Fig. 1 A**). This sharp onset of polarized flow makes the *Drosophila* embryo a powerful system to study the physical mechanisms that drive tissue flow.

It is so far unclear what creates this early polarized flow in the *Drosophila* embryo. One possibility is that it might be coupled to and dependent on other processes during early *Drosophila* morphogenesis, such as mesoderm invagination on the ventral side (10), germband extension along the lateral side (16), or the cephalic furrow in the anterior (27). Indeed, existing studies have shown that most of the embryonic tissue flow can be accurately predicted from the pattern of non-muscle Myosin-II (hereafter myosin) localization and polarization (28). However, earlier studies revealed that an additional force arising near the posterior pole must contribute to driving tissue flows, as evidenced by gradients of cell shape (16, 26) and mechanical stresses (16), as well as genetic and mechanical perturbations (16, 29). For instance, blocking endoderm invagination (as in a *Torso* mutant) entirely blocks whole-embryo elongation (16). Moreover, the early polarized flow of the endoderm is independent of the above-mentioned processes, as demonstrated by embryos with simultaneously blocked mesoderm invagination (*twist, snail* (30)), germband extension, and cephalic furrow formation (*eve* (31); **Movie S2**, **Fig. S1 A, B**). Hence, the question remains as to what causes the first polarized tissue flow of the *Drosophila* epithelium and initiation of axis elongation.

Results

Drosophila morphogenesis begins with symmetric tissue flow that becomes polarized

To understand what drives tissue flow in early *Drosophila* morphogenesis, we first quantified the flow to determine how it evolves in time. To do so, we performed live imaging of *Drosophila* embryos using a two-photon microscope to capture the sagittal plane that cuts through the center of the embryo (**Fig. 1 B, C**, **Materials and Methods**). We tracked the position of the pole cells (pos_{pc}) to quantify the motion of the posterior tissue (**Movie S3**, **Materials and Methods**), which revealed that there is an initially slow flow of the posterior, which speeds up over time (**Fig. 1 D**).

We also quantified the spatial profile of the flow in the epithelium by performing particle image velocimetry (PIV) on subsequent frames and extracting the velocity of the flow tangential to the midline of the epithelium (v; **Fig. 1 B, C**, **Materials and Methods**). At each time, the tangential velocity (**Fig. 1 E**) can be spatially averaged to give a single value that describes the global polarity of the flow ($\bar{v}$; **Fig. 1 F**). If there is as much clockwise (positive) flow as counterclockwise (negative) flow, the average is zero, and the flow is

considered symmetric (as at T_{cell} = 9 min). If there is more clockwise flow than counterclockwise flow, the average will be positive, indicating that the flow is polarized (as at T_{cell} = 17 min). Averaging the velocity revealed that there are two distinct phases of flow: a symmetric flow for approximately the first twelve minutes after the cellularization front passes the nuclei (T_{cell} = 0, **Materials and Methods**), followed by the onset of polarized flow with average velocity that increases in time (**Fig. 1 F**).

When we performed the same quantifications on embryos mutant for *eve*, *twist*, and *snail* (hereafter *ets*), which have blocked mesoderm invagination, germband extension, and cephalic furrow formation (**Movie S2**, **Fig. S1 A, B**), we still saw this transition to polarized flow (**Fig. S1 C, D**). The timing of the transition was even slightly earlier in *ets* embryos than in wildtype, likely due to the lack of ventral pulling from the mesoderm invagination, as evidenced by the increased flow in the ventral-anterior region of the embryo ($-0.2 < s < 0$; **Fig. S1 E, F**). This clearly demonstrates that the polarized flow does not depend on myosin polarization in the germband, or on geometric constraints imposed by the cephalic furrow as previously predicted (27, 28). This lead us to two main questions: What physical mechanisms drive tissue flow in the early *Drosophila* embryo? And what mechanism is involved in the transition from symmetric to polarized flow?

Symmetric and polarized tissue flows arise from basal and apical myosin respectively

Myosin is known to be a common tissue-intrinsic driver of flow in many biological tissues (1, 32). We therefore imaged the myosin distribution in the embryo as a function of time to determine its impact on tissue flow. In wildtype embryos (**Fig. 2 A** top row), there are two distinct populations of myosin: one on the apical side of the cells, and the other on the basal side.

During the symmetric phase of flow, there is no apical myosin activation, but there is a strong accumulation of basal myosin (**Fig. 2 A** top left), associated with the process of cellularization (25). Cellularization completes first on the ventral side of the embryo, causing more basal myosin dorsally than ventrally (**Fig. 2 B**), which coincides with the center of the domain of symmetric tissue flow (**Fig. S2 A**). This lead us to the hypothesis that non-uniformity of basal myosin could drive the symmetric phase of tissue flow, as previously proposed (28).

To test this hypothesis, we used a mutation that removes the dorsal-ventral specification of the embryo, and leads the entire embryo to act as ventrolateral tissue (33) (*toll*^{rm9}/*toll*^{rm10} hereafter *toll vl*; **Fig. 2 A** middle row). This makes the embryo rotationally symmetric about its anterior-posterior axis (**Fig. S2 B**), which in turn removes the dorsal-ventral difference in basal myosin (**Fig. 2 B**, **Movie S5**). In *toll vl* embryos, the posterior tissue does not always flow dorsally, but instead is significantly more likely than wildtype to flow towards the ventral or lateral directions (**Fig. S2 C**, **Movie S4**). To quantify the flow in the imaging plane, we analyzed only embryos that flow dorsally. Tracking the pole cells in these mutants revealed that the early, symmetric flow is almost completely halted (**Fig. 2 D**), confirming that the symmetric flow observed is driven by the increased activation of basal myosin on the dorsal side of the embryo.

We next considered what drives the polarized flow that occurs following the symmetric phase of flow. Around the time where the transition occurs, the levels of basal myosin begin to decrease and there is a localized accumulation of apical myosin in the dorsal posterior (**Fig. 2 A top right, C**). To test whether the polarized flow requires this posterior pool of apical myosin, we strongly downregulated all apical myosin in the embryo using a mutation in the gene encoding for the G protein $G\alpha_{12/13}$ (known as Concertina (Cta) in *Drosophila*), which is required specifically for medial apical myosin recruitment (34, 35) (**Fig. 2 A** bottom row, **Movie S5**). Quantifying the flow by pole cell tracking (**Fig. 2 D**) and by averaging epithelial velocity (**Fig. 2 E**) showed that the symmetric flow is similar to wildtype, but that the polarized flow is strongly suppressed.

Based on these observations, we concluded that the symmetric phase of flow requires the nonuniformity of basal myosin and the polarized flow requires apical myosin. Since polarized tissue flow is normal in *ets* mutants in which mesoderm invagination and germband extension are blocked, we concluded that apical myosin is required strictly in the posterior region of the embryo and not in other adjacent tissues. It is known that the main effect of myosin accumulation is to drive contraction of the acto-myosin network inside of cells (1, 32). We therefore decided to investigate whether the observed flow dynamics arise solely due to tissue contraction driven by these two different pools of myosin.

Myosin-driven tension-based model explains the symmetric flow

To gain mechanistic insight into the process driving the flow, we decided to test our hypotheses using a combination of experiments and modeling. Our aim was to understand the embryo flow dynamics on the tissue scale, we therefore chose to use a model that considers collective cellular behavior rather than individual cellular processes. Because the strain rates measured during this phase of development do not surpass approximately 1/50 min^{-1} (**Fig. S3 A, B**), we neglected elastic stresses, which are expected to relax much faster, on the time scale of approximately 2-5 min (36). Finally, we focused on the flow within a sagittal section of the embryo, which we described by a continuous, thin 1D membrane. These simplifications allowed us to compare our sagittal observations of embryos in two-photon microscopy to a model of a 1D thin active fluid (37, 38) (***SI Appendix***), which takes into account tissue viscosity, friction with the vitelline membrane (part of the eggshell that surrounds the embryo), and myosin-driven spatially-dependent active tension (equation (1) in **Fig. 3 A**).

This type of model is effective for making quantitative comparisons as well as qualitative predictions. To quantitatively compare our model to the data, we solved equation (1) for velocity, using the measured apical and basal myosin intensities (both in symmetric and polarized phase of flow, **Fig. 3 B** and **Fig. 3 D** respectively) as input to the equation. By fitting to the measured velocity field, we extracted the values of three relevant physical parameters (***SI Appendix***). The first parameter is a hydrodynamic length scale $l_H = \sqrt{\eta/\gamma}$, which reflects the ratio between viscosity, η, and friction with the surroundings, γ. The other two parameters are conversion factors that relate myosin intensity to active tension (f_a for apical myosin and f_b for basal myosin), which are divided by viscosity η. The resulting ratios, r_a and r_b, reflect tissue contraction rates for apical and basal myosin respectively. To build qualitative intuition, we also performed simulations of a simplified model without basal myosin on an elliptic representation of the embryo (hereafter elliptic model), using values of the relevant physical parameters from our fitting (***SI Appendix***).

We then used this model to test our hypothesis that the non-uniform contraction of basal myosin is what drives the observed symmetric flow. To simplify our modeling studies, we chose to use *ets* instead of wildtype embryos. *ets* embryos behave similarly to wildtype at early times but do not have a mesoderm invagination (**Fig. S1)**, which is a separate complex process of flow and deformation that we do not model explicitly. We first averaged the data over all *ets* embryos where, to decrease embryo-to-embryo variation,

we aligned the embryos to the time at which each transitioned to polarized flow (T_{asb} = 0; **Fig. S4).** We performed a fit of the model given by equation (1) to the data with l_H, r_a, and r_b as free parameters, and found that we could reproduce the symmetric flow (**Fig. 3 C**). However, this model could not reproduce the later polarized flow (**Fig. 3 E**) because the spatially averaged velocity is always strictly zero for this simple model (**Fig. 3 F**). Non-zero average flow is not possible because equation (1) contains only tissue-intrinsic, symmetric forces and a homogeneous friction force, none of which can lead to polarized flow. Thus, an additional mechanism is required for driving the polarized flow.

Localized friction or adhesion is not responsible for polarized flow

During the polarized phase of flow, the dorsal-posterior activation of apical myosin (**Fig. 2 A, 3 D**) leads to bending of the epithelium. This causes the anterior end of the apical myosin domain to come into close contact with the eggshell (29), which could create a localized domain with higher friction. This close contact could also lead to adhesion between the epithelium and the eggshell due to the presence of the adhesion protein alpha-Integrin (Scab), which is expressed in this region (39). Intuitively, this configuration could lead to asymmetric contraction of the myosin patch since one end is able to move more freely than the other. Adhesion of the anterior end of the apical myosin domain has even been shown to be crucial to the anterior wave propagation of the endoderm invagination slightly later in development (29). To test whether the polarized flow that we observe could be created by such an asymmetric friction, we accordingly updated our model by including a domain (G) that translocates at the anterior end of the myosin domain, where friction is increased by a factor g (see equation (2) in **Fig. 4 A)**.

To build intuition for the effect of this new term in the model, we performed simulations using our elliptic model (**Fig. S5 A, B**). We obtained polarized flow, though the average velocity remained constant in time unless the amount of localized friction g (**Fig. 4 B**) or the myosin intensity (**Fig. 4 C**) changed over time. The latter could be a possibility as our observed data shows apical myosin increasing over time (**Fig. 2 C**).

To test the localized-friction model against the experimental data, we performed detailed fits of the measured velocity to solutions of equation (2) using the measured time-dependent apical and basal myosin patterns, where we included the additional fit parameter g, which we restricted to be positive. While we

found that this reproduced the observed overall increase in the spatially average velocity (**Fig. 4 D**), it failed to predict the observed spatial velocity profile at individual time points (**Fig. 4 E**, corresponding fitting with a time-dependent localized friction *g* resulted in a similar outcome **Fig. S5 C, D**). This is because the model predicts that, for positive values of *g*, the velocity in region *G* should be negative (counter clockwise) or go to zero in the case of infinite friction (as shown using our elliptic model in F**ig. S5 F**, ***SI Appendix***), while experimentally we observed positive (clockwise) flow.

We also experimentally tested the contributions of alpha-Integrin-mediated adhesion to polarized flow, by generating a CRISPR knock-out of *scab* (39) (**Movie S6**). We found that the movement of the posterior tissue is almost identical for wildtype and *scab* embryos (**Fig. S5 G**), however the average velocity after symmetry breaking is reduced for *scab* mutants (**Fig. 4 F**). To reduce the impacts of any unintended effects of the mutation on other parts of the embryo (**Fig. S5 H),** we also computed a spatially averaged velocity over only the posterior domain of the epithelium ($\bar{v}_{pos}$; **Fig. 4 G**). This analysis confirmed that the onset of polarized flow in *scab* mutant embryos is similar to wildtype, thus indicating that alpha-Integrin is not required for the onset of polarized flow. Taken together, our combined study of modeling and experiment ruled out adhesion (or localized friction) as a mechanism for the onset of polarized flow.

Interaction of tissue curvature with active moment can explain the polarized flow

Polarized forces, and thus polarized flow, can be created by the interaction of a curvature gradient with an active moment, which follows from the theory of active surfaces (40) (***SI Appendix***). Active moments are created when apical and basal myosin tensions differ. When myosin (and therefore active tension) is present at similar levels apically and basally in a region of tissue, this acts to contract the green region, which in turn exerts forces on the surrounding tissue (**Fig. 5 A**). When the levels of apical and basal myosin differ in a region of tissue, an active moment is present that causes this region to exert torques on neighboring tissue, which acts to increase or decrease the curvature of the green region (**Fig. 5 B**).

We therefore hypothesized that polarized flow could arise because the dorsal-posterior apical myosin patch creates an active moment that interacts with the curvature gradient in this region**.** The emergence of polarized flow can be most clearly explained in the limit where the yolk pressure is so high that it presses

the epithelium against the eggshell. In this case, the epithelium is forced to have the same curvature as the eggshell everywhere. Since the region with the apical myosin patch has a positive active moment, it will act to decrease its own curvature, which happens only if it moves away from the pole, creating polarized flow (**Fig. 5 C**).

To test whether this effect could explain our observations, we added coupling between the active moment and the epithelium curvature to our quantitative model by including a new force term, as shown in equation (3) (**Fig. 5 D, *SI Appendix***). This term follows directly from the theory of active surfaces (40), and includes no new fit parameters. The resulting flow depends critically on the position of the domain of apical myosin activation, relative to the curvature profile of the embryo. A simple quantity to consider is the offset between the center of the apical myosin domain and the position of peak epithelial curvature at the posterior pole (henceforth called myosin-curvature offset, s_{off}, **Fig. 5 E**). Simulating equation (3) using our elliptic model (**Fig. S6 A, B**) created polarized flow where the average velocity increased as s_{off} increased (**Fig. 5 F**) even when we held the myosin intensity constant over time.

To further test our hypothesis, we fit equation (3) to the experimentally measured velocity patterns, using measured myosin and curvature data. Fitting with all physical parameters held constant over time reproduced the substantial increase of the polarized flow with time, but also predicted some polarized flow at times before symmetry breaking (blue curve **Fig. 5 G, H**). We found that this early polarized flow in the blue fit curve arises due to the active moment created by basal myosin (**Fig. S6 C**). This suggested that there must be something that prevents polarized flow at early stages. It has previously been observed that the amount of friction changes over time during the early phase of cellularization in the *Drosophila* embryo (36). Moreover, tissue deformations and folding that occur during gastrulation alter the distance between epithelium and eggshell in certain regions, which could further affect the friction. Accordingly, we performed fitting allowing the overall homogeneous friction, γ, to change over time. This modified fit captured the experimentally observed transition from symmetric to polarized flow and the spatial velocity patterns (magenta curves, **Fig. 5 G, H**). This fit suggested a large increase of the hydrodynamic length l_H around the time of symmetry breaking, i.e. a large decrease in friction with the eggshell (**Fig. S6 D**). However, this increase in l_H decreased drastically when we consider that the region expressing apical myosin can only be

compressed by a finite amount (**Fig. S6 E, F** and **Fig. S7**, ***SI Appendix***). Comparing fitting accuracies using chi-squared analysis, we found that the curvature-active-moment model, equation (3), could consistently explain the measurements better than the tension-with-heterogeneous-friction model, equation (2) (**Fig. 5 I**). This supports the idea that coupling between curvature and active moment can act as a driver for the polarized flow observed in the early embryo.

Changing embryo curvature and active moment alters the flow, consistent with the model

To further test the predictions of the model, we performed targeted perturbations to parameters that are essential for flow in the model: the curvature of the embryo, and the location of the apical myosin domain with respect to the curvature peak (s_{off}).

To alter the curvature of the embryo, we took advantage of the fact that there is an adhesion molecule, Fat2, present in the maternal follicular epithelium that is needed to shape embryo geometry. We therefore used *UAS-fat2-RNAi, traffic jam(tj)-GAL4* mothers to produce embryos with altered shape (41–43) (hereafter *fat2* embryos) that are significantly shortened along the anterior-posterior axis and, as a result, are much rounder (**Fig. 6 A, B, Movie S7**). To explore the expected impact of changing the aspect ratio on the flow dynamics, we performed simulations based on equation (3) using our elliptic model with varying aspect ratios. The simulations predicted that decreasing the embryo's aspect ratio should decrease the rate at which the spatially averaged velocity increases during the phase of polarized flow (**Fig. 6 C**). Experimentally, we observed a wide variation in the average velocity profile for individual *fat2* embryos (**Fig. S8 A**). But, when the embryos were aligned with respect to the onset of polarized flow, we observed the predicted decrease in the average velocity (**Fig. 6 D**). This decreased velocity was confirmed by tracking of the position of the posterior tissue (**Fig. 6 E**) and by averaging the velocity in only the posterior of the embryo (**Fig. S8 B**). This result confirms that the geometry of the embryo, plays an important role in the onset and the dynamics of the polarized flow.

Next, we altered the position of the apical myosin domain using the *toll vl* mutant embryos described previously. Because the *toll vl* mutation removes dorsal-ventral polarity, the domain of apical myosin becomes more centered on the posterior pole of the embryo compared to the dorsal-posterior localization

in wildtype (**Fig. 6 F, G**). The difference becomes increasingly significant over time. According to our prediction, decreasing the myosin-curvature offset, s_{off}, is expected to decrease the average velocity (**Fig. 5 G**). Once the individual embryos (**Fig. S8 C**) were aligned with respect to the onset of polarized flow, this decrease in the average velocity was confirmed experimentally (**Fig. 6 D**, **E**, **Fig. S8 B**).

In addition to the decrease in average velocity, there is a large delay (approximately 5 min) in the onset of polarized flow in *toll vl* embryos (**Fig. 2 E**). This delay likely occurs for two reasons. If the apical myosin patch were perfectly centered on the posterior pole, it would not flow at all until it was displaced slightly in any direction by some other effect. This would also explain why *toll vl* embryos tend to flow in directions other than dorsally as normally seen in wildtype (**Fig. S2**). Additionally, *toll vl* embryos lack the dorsal-ventral asymmetry in basal myosin that, in wildtype embryos, leads the myosin patch to shift away from the pole even before the onset of polarized flow. This initial shift increases the speed of polarized flow arising from the myosin-curvature offset in wildtype. There is, in a sense, a feedback based on the initial position of the apical myosin patch and the initial flow. The larger the offset, the more polarized flow, which increases the offset, and so on until the domain of myosin reaches the region of lowest curvature on the dorsal side of the embryo.

We performed two further tests to assess whether the observed change in flow results from the changed position of myosin with respect to the curvature peak. First, we extracted parameters from wildtype fitting (**Fig. S9 A, B**), and used the myosin and curvature profiles measured in *toll vl* to predict flow using model equation (3). This prediction yielded a good match to the experimentally measured flows in *toll vl* embryos and confirmed the decrease in the average velocity (**Fig. S9 C, D**). Secondly, we quantified flow dynamics in *capicua* mutant embryos, whose apical myosin domain is larger but more centered on the posterior pole than in wildtype embryos (**Fig. S8 D, E**, **Movie S8**). In *capicua* embryos we observed a slowed and delayed increase in average velocity despite a larger domain of apical myosin (**Fig. S8 F, G**), which was also predicted by simulations using our elliptic model (**Fig. S8 H**).

Taken together, these experimental perturbations deeply and broadly challenge the predictions of the model. We therefore conclude that the model given in equation (3) accurately captures the features that

are necessary for driving the onset and evolution of polarized flow in early *Drosophila* morphogenesis. Overall, our results show that an initially symmetric flow, driven by a non-uniform pool of basal myosin, transitions to polarized flow as a result of the activation of apical myosin in a domain of the embryo that experiences a curvature gradient.

Discussion

We have identified two distinct phases of tissue flow in the early *Drosophila* embryo, where an initially symmetrically deforming tissue gradually transits to a polarized flow. While previous work has studied flow-generating mechanisms during morphogenesis, we showed that this polarized flow can neither be explained by forces emerging from other tissues such as the germband and mesoderm (**Fig. S1**), nor by a myosin-adhesion coupling. Our work revealed instead that a coupling between tissue curvature and an active moment, generated by a difference in apical and basal myosin intensity, is responsible for driving the polarized flow. We also demonstrated the importance of spatially varying curvature, with an offset between the curvature peak and the domain of the active moment for early polarized movement.

This system is an ideal example for how organized multicellular dynamics that occur during morphogenesis emerge from inherited genetic, and geometric blueprints inherited from the mother. Beyond simply fulfilling inherited instructions, the offset between the patterns of cell contractility and tissue curvature is also amplified by the very flow it induces. This illustrates that interactions between genetic and geometric information update this information as a result of morphogenesis. Thus, information is not simply inherited, it is constantly modified.

While the mechanism that we report accurately describes the onset of polarized flow, it is not sufficient to explain later stages of flow, as the decreased curvature gradient towards the dorsal side of the embryo is unfavorable for sustained flow. Indeed, it has been shown that later phases of flow do depend on the process of germband elongation, driven by myosin polarization in the lateral ectoderm (14–16), and on dynamically regulated adhesion between the epithelium and the vitelline membrane in the dorsal posterior(29).

To keep our model as simple as possible while still revealing the mechanisms required to achieve the observed flow, we restricted our investigation to the 1D tangential flow in the sagittal plane of the epithelium and made several simplifying assumptions. Quantitative comparisons of the model to our data suggested that contraction of the tissue in the primordium is limited by elastic resistance, which for simplicity, we modeled by a local increase in viscosity (**Fig. S7**). This is consistent with the fact that, due to the incompressibility of the cytoplasm, there is a limit to cell deformation upon contraction (**Movie S1)**. However, for a complete understanding of tissue flow, deformation, and folding, explicit consideration of elasticity and a full 3D modeling approach will be necessary. This would open the way to addressing for example how tissue flow progresses along the dorsal midline during later stages of embryo development.

Morphogenetic processes are both self-organized and dependent upon initial conditions to deterministically guide future processes (2). In *in vitro* synthetic systems, such initial conditions are engineered to drive robust organoid development (44, 45), but *in vivo* they are inherited from previous developmental stages. During development, heredity is classically associated with genomic heredity. Yet, as we show here, structural or geometric heredity (eg. egg size and shape) is also essential to drive tissue flow and morphogenesis. It will be interesting to investigate further how the interplay between genetic and geometric heredity guide developmental processes in other systems.

Materials and Methods

Fly strains and genetics

Details of the fly lines used are provided in the Supporting Information.

Sample preparation

Flies were kept in a cage at 25°C with the exception of GAL4 lines which were kept at 18°C. Embryos were collected using apple cider plates smeared with yeast paste. Embryos were transferred to a mesh basket, rinsed with water, dechorionated with 2.6% bleach for 1 min, then rinsed copiously with water before being transferred back to clean agar. Embryos in the early stages of cellularization were visually selected, and aligned laterally. They were then transferred to a glass coverslip coated with homemade glue. A drop of Halocarbon 200 Oil (Polysciences; for DIC experiments) or 1x phosphate buffered saline (prepared from

Dulbecco's phosphate buffered saline (eurobio); for two photon experiments) was placed on the embryos to keep them from drying during imaging.

Brightfield imaging

For quantifying the direction of tissue rotation in *toll vl* mutants (**Fig. S2 C**), embryos were imaged at 21°C on a Zeiss Axiovert 200M inverted microscope using a 20x-0.75 numerical aperture (NA) objective. Images were acquired once per minute for 2-3 hours.

Two photon imaging

For all other experiments, embryos were imaged at 23.5-24.5°C using a Nikon A1R MP+ multiphoton microscope with a 25x-1.10 NA water-immersion objective. Illumination was provided by a pulsed 1040 nm laser (Coherent) for mScarlet and tunable wavelength pulsed laser (Coherent) set to 920 nm for GFP. Images were acquired once every 30 seconds with 2x line averaging.

Data Analysis

Pole cell tracking

We selected a central pole cell and manually tracked its coordinates over time in FIJI. As the selected pole cell began to invaginate, we tracked the position radially outwards from it near the vitelline membrane to record only its tangential movement (**Movie S3**). The position is defined as $pos_{pc} = \sqrt{(x - x_o)^2 + (y - y_o)^2}$ where (x_o, y_o) is the position at $T_{cell} = 0$.

Image analysis

The two photon images were processed using custom python scripts to align and segment the embryos, and to extract the apical and basal myosin profiles. See the Supporting Information for a full description of the procedure.

Acknowledgements

We thank all members of the Lecuit group for useful discussions. We thank Marc-Eric Perrin for help with machine learning used for embryo segmentation; Claudio Collinet for help conceiving the project and for preliminary experiments and fly work; and Jean-Marc Philippe, Elise da Silva, and Maxime Louis for

designing and generating the molecular constructs used. We thank the Bloomington for providing fly stocks and the IBDM animal facility. M.M. thanks the Centre Interdisciplinaire de Nanoscience de Marseille (CINaM) for providing office space.

E.W.G. and B.C. were supported by the European Research Council Advanced Grant SelfControl 788308 awarded to T.L. T.L. is supported by the Collège de France. M.M. received funding from the Turing Center for Living Systems (CENTURI), funded by France 2030, the French Government program managed by the French National Research Agency (ANR-16-CONV-0001), and from Excellence Initiative of Aix-Marseille University - A*MIDEX. The IBDM imaging platform and the France-BioImaging infrastructure supported by the Agence Nationale de la Recherche (ANR-10-INSB-04-01 ; call “Investissements d’Avenir”) provided support.

Data and materials availability

The datasets generated and/or analyzed during the current study are available from the corresponding authors on reasonable request. The computer code used to perform data analysis, simulations, and model fitting is available from the corresponding authors on reasonable request.

References

1. M. Murrell, P. W. Oakes, M. Lenz, M. L. Gardel, Forcing cells into shape: the mechanics of actomyosin contractility. *Nat Rev Mol Cell Biol* **16**, 486–498 (2015).

2. C. Collinet, T. Lecuit, Programmed and self-organized flow of information during morphogenesis. *Nat Rev Mol Cell Biol* **22**, 245–265 (2021).

3. T. Lecuit, P.-F. Lenne, Cell surface mechanics and the control of cell shape, tissue patterns and morphogenesis. *Nat Rev Mol Cell Biol* **8**, 633–644 (2007).

4. J.-Y. Lee, *et al.*, Wnt/Frizzled signaling controls *C. elegans* gastrulation by activating actomyosin contractility. *Curr Biol* **16**, 1986–1997 (2006).

5. M. Roh-Johnson, *et al.*, Triggering a cell shape change by exploiting preexisting actomyosin contractions. *Science* **335**, 1232–1235 (2012).

6. A. C. Martin, M. Kaschube, E. F. Wieschaus, Pulsed contractions of an actin–myosin network drive apical constriction. *Nature* **457**, 495–499 (2009).

7. L. A. Davidson, M. A. Koehl, R. Keller, G. F. Oster, How do sea urchins invaginate? Using biomechanics to distinguish between mechanisms of primary invagination. *Development* **121**, 2005–2018 (1995).

8. K. Sherrard, F. Robin, P. Lemaire, E. Munro, Sequential activation of apical and basolateral contractility drives ascidian endoderm invagination. *Curr Biol* **20**, 1499–1510 (2010).

9. A. C. Martin, B. Goldstein, Apical constriction: themes and variations on a cellular mechanism driving morphogenesis. *Development* **141**, 1987–1998 (2014).

10. M. Rauzi, *et al.*, Embryo-scale tissue mechanics during *Drosophila* gastrulation movements. *Nat Commun* **6**, 8677 (2015).

11. B. Guirao, *et al.*, Unified quantitative characterization of epithelial tissue development. *eLife* **4**, e08519 (2015).

12. R. Etournay, *et al.*, Interplay of cell dynamics and epithelial tension during morphogenesis of the *Drosophila* pupal wing. *eLife* **4**, e07090 (2015).

13. Y. Gong, C. Mo, S. E. Fraser, Planar cell polarity signalling controls cell division orientation during zebrafish gastrulation. *Nature* **430**, 689–693 (2004).

14. C. Bertet, L. Sulak, T. Lecuit, Myosin-dependent junction remodelling controls planar cell intercalation and axis elongation. *Nature* **429**, 667–671 (2004).

15. J. T. Blankenship, S. T. Backovic, J. S. P. Sanny, O. Weitz, J. A. Zallen, Multicellular rosette formation links planar cell polarity to tissue morphogenesis. *Dev Cell* **11**, 459–470 (2006).

16. C. Collinet, M. Rauzi, P.-F. Lenne, T. Lecuit, Local and tissue-scale forces drive oriented junction growth during tissue extension. *Nat Cell Biol* **17**, 1247–1258 (2015).

17. E. Rozbicki, *et al.*, Myosin-II-mediated cell shape changes and cell intercalation contribute to primitive streak formation. *Nat Cell Biol* **17**, 397–408 (2015).

18. D. S. Adams, R. Keller, M. A. Koehl, The mechanics of notochord elongation, straightening and stiffening in the embryo of *Xenopus laevis*. *Development* **110**, 115–130 (1990).

19. A. Shindo, J. B. Wallingford, PCP and septins compartmentalize cortical actomyosin to direct collective cell movement. *Science* **343**, 649–652 (2014).

20. Q. Lu, P. Bhattachan, B. Dong, Ascidian notochord elongation. *Dev Biol* **448**, 147–153 (2019).

21. A. Shindo, Models of convergent extension during morphogenesis. *Wiley Interdiscip Rev Dev Biol* **7**, e293 (2018).

22. B. Aigouy, *et al.*, Cell flow reorients the axis of planar polarity in the wing epithelium of *Drosophila*. *Cell* **142**, 773–786 (2010).

23. R. P. Ray, *et al.*, Patterned anchorage to the apical extracellular matrix defines tissue shape in the developing appendages of *Drosophila*. *Dev Cell* **34**, 310–322 (2015).

24. M. Saadaoui, D. Rocancourt, J. Roussel, F. Corson, J. Gros, A tensile ring drives tissue flows to shape the gastrulating amniote embryo. *Science* **367**, 453–458 (2020).

25. A. Mazumdar, M. Mazumdar, How one becomes many: Blastoderm cellularization in *Drosophila* melanogaster. *BioEssays* **24**, 1012–1022 (2002).

26. C. M. Lye, *et al.*, Mechanical coupling between endoderm invagination and axis extension in *Drosophila*. *PLOS Biol* **13**, e1002292 (2015).

27. M. Dicko, *et al.*, Geometry can provide long-range mechanical guidance for embryogenesis. *PLOS Comp Biol* **13**, e1005443 (2017).

28. S. J. Streichan, M. F. Lefebvre, N. Noll, E. F. Wieschaus, B. I. Shraiman, Global morphogenetic flow is accurately predicted by the spatial distribution of myosin motors. *eLife* **7**, e27454 (2018).

29. A. Bailles, *et al.*, Genetic induction and mechanochemical propagation of a morphogenetic wave. *Nature* **572**, 467–473 (2019).

30. M. Leptin, *twist* and *snail* as positive and negative regulators during *Drosophila* mesoderm development. *Genes Dev* **5**, 1568–1576 (1991).

31. K. D. Irvine, E. Wieschaus, Cell intercalation during *Drosophila* germband extension and its regulation by pair-rule segmentation genes. *Development* **120**, 827–841 (1994).

32. P. Chugh, *et al.*, Actin cortex architecture regulates cell surface tension. *Nat Cell Biol* **19**, 689–697 (2017).

33. D. S. Schneider, K. L. Hudson, T. Y. Lin, K. V. Anderson, Dominant and recessive mutations define functional domains of Toll, a transmembrane protein required for dorsal-ventral polarity in the *Drosophila* embryo. *Genes Dev* **5**, 797–807 (1991).

34. S. Parks, E. Wieschaus, The *Drosophila* gastrulation gene concertina encodes a Gα-like protein. *Cell* **64**, 447–458 (1991).

35. S. Kerridge, *et al.*, Modular activation of Rho1 by GPCR signalling imparts polarized myosin II activation during morphogenesis. *Nat Cell Biol* **18**, 261–270 (2016).

36. A. D'Angelo, K. Dierkes, C. Carolis, G. Salbreux, J. Solon, In vivo force application reveals a fast tissue softening and external friction increase during early embryogenesis. *Curr Biol* **29**, 1564-1571.e6 (2019).

37. S. Münster, *et al.*, Attachment of the blastoderm to the vitelline envelope affects gastrulation of insects. *Nature* **568**, 395 (2019).

38. M. Mayer, M. Depken, J. S. Bois, F. Jülicher, S. W. Grill, Anisotropies in cortical tension reveal the physical basis of polarizing cortical flows. *Nature* **467**, 617–621 (2010).

39. K. A. Stark, *et al.*, A novel alpha integrin subunit associates with betaPS and functions in tissue morphogenesis and movement during *Drosophila* development. *Development* **124**, 4583–4594 (1997).

40. G. Salbreux, F. Jülicher, Mechanics of active surfaces. *Phys Rev E* **96**, 032404 (2017).

41. S. Horne-Badovinac, J. Hill, G. Gerlach II, W. Menegas, D. Bilder, A screen for round egg mutants in *Drosophila* identifies Tricornered, Furry, and Misshapen as regulators of egg chamber elongation. *G3* **2**, 371–378 (2012).

42. K. Barlan, M. Cetera, S. Horne-Badovinac, Fat2 and Lar define a basally localized planar signaling system controlling collective cell migration. *Dev Cell* **40**, 467-477.e5 (2017).

43. I. Viktorinová, T. König, K. Schlichting, C. Dahmann, The cadherin Fat2 is required for planar cell polarity in the *Drosophila* ovary. *Development* **136**, 4123–4132 (2009).

44. M. Hofer, M. P. Lutolf, Engineering organoids. *Nat Rev Mater* **6**, 402–420 (2021).

45. B. H. Lee, I. Seijo-Barandiaran, A. Grapin-Botton, Epithelial morphogenesis in organoids. *Curr Opin Genet Dev* **72**, 30–37 (2022).

46. O. Ronneberger, P. Fischer, T. Brox, U-net: Convolutional networks for biomedical image segmentation (2015) https:/doi.org/10.48550/arXiv.1505.04597 (July 4, 2022).

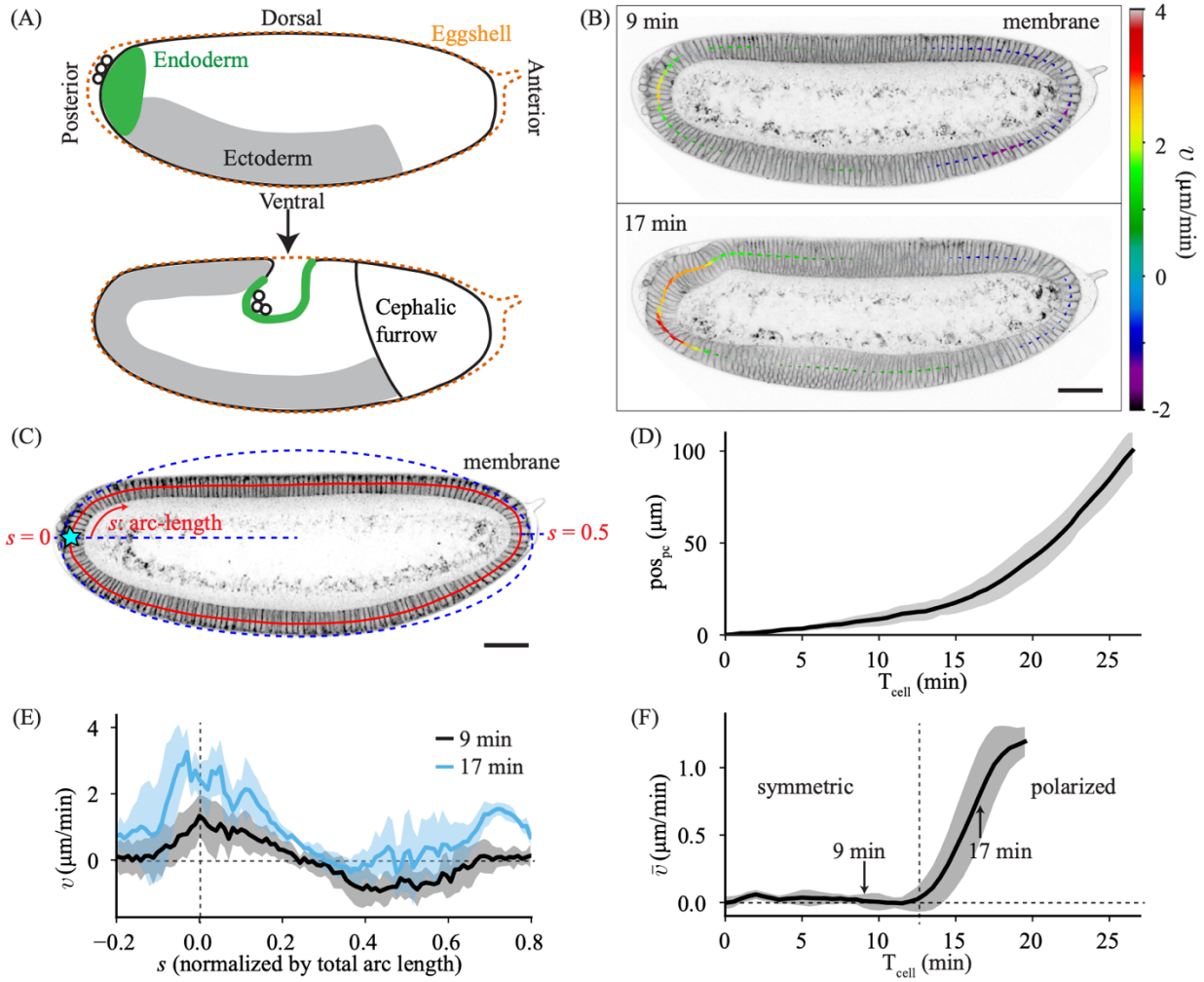

Fig. 1. Quantification of tissue flow during early *Drosophila* morphogenesis. (A) Cartoons of *Drosophila* embryo (*top*) at an early stage, during cellularization, and (*bottom*) approximately 30 minutes later. **(B)** Sagittal plane of an embryo imaged with membrane marker GAP43::mScarlet at 9 minutes and 17 minutes after the cellularization front passes the nuclei in the dorsal posterior (T_{cell} = 0). The arrows show the tangential velocity of the tissue along the midline, extracted using particle image velocimetry. **(C)** Two-photon images of the sagittal plane of an embryo imaged with GAP43::mScarlet. The red line denotes the midline of the epithelium. The arc-length (*s*) increases in the clockwise direction and is normalized to the total length of the midline. The blue dashed line represents an elliptical fit to the apical surface of the epithelium, used to determine the location of *s* = 0 at the posterior pole (see **Materials and Methods**). **(D)** Quantification of the pole cell position (pos_{pc}, see **Materials and Methods**) as a function of time after T_{cell}

= 0, averaged over 6 embryos. **(E)** Spatial profile of tangential tissue velocity along the midline at the same times as in **C**, averaged over 5 embryos. **(F)** Spatial average of the tangential velocity ($\bar{v}$) as a function of time. Vertical dashed line marks the onset of polarized flow. Average performed over 5 embryos. All scale bars are 50 μm. Error bars represent the standard deviation.

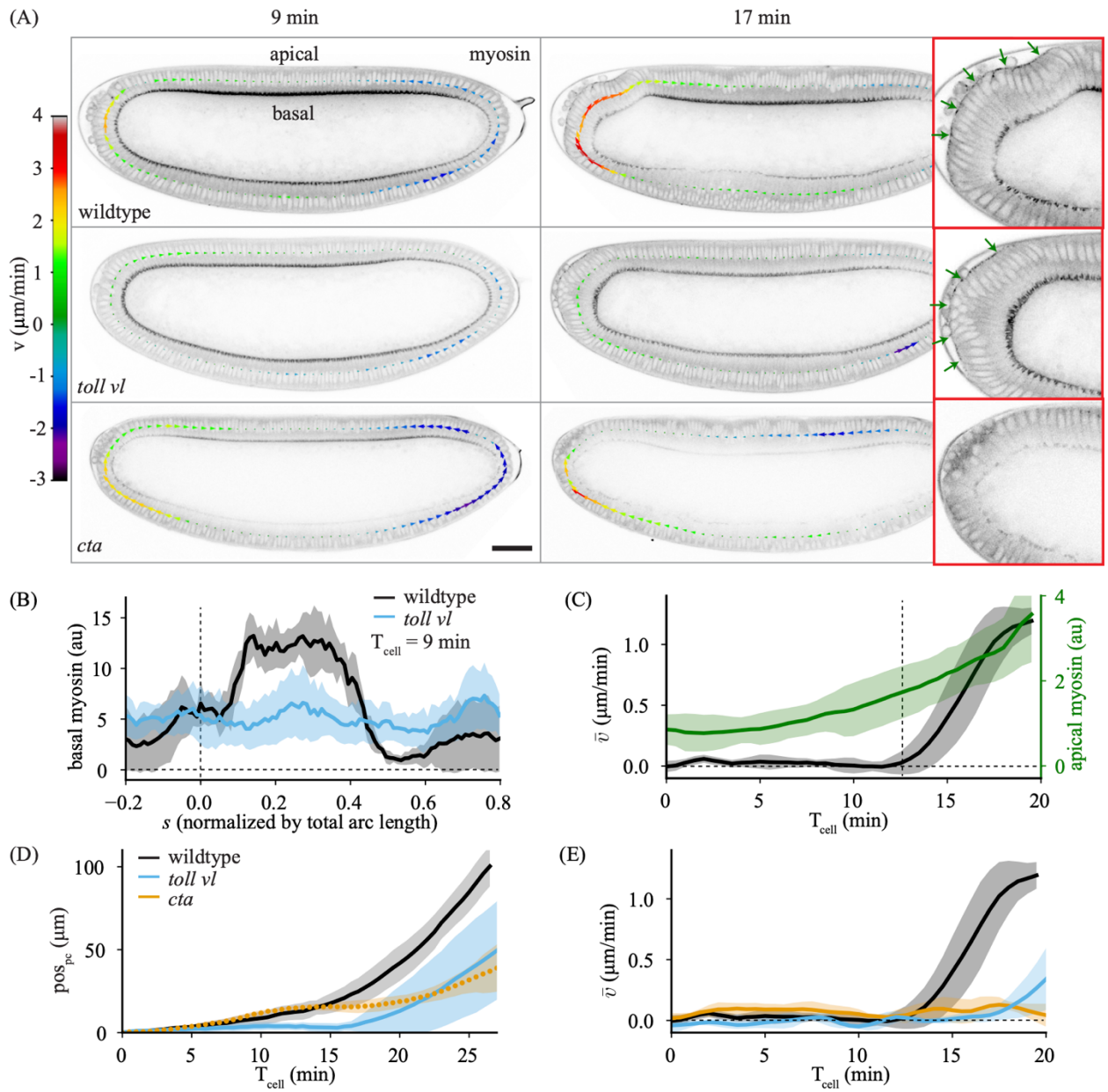

Fig. 2. Impact of apical and basal myosin on tissue flow. (A) Sagittal plane of an embryo imaged with Myosin-II (myosin) marker *spaghetti squash* (*sqh*)::GFP at 9 minutes and 17 minutes after T_{cell} = 0 for (*top*) wildtype, (*middle*) *toll vl* mutant, and (*bottom*) *cta* mutant embryos. The arrows show the tangential velocity of the tissue along the midline. The panels on the right show a zoomed view of the posterior at T_{cell} = 17 min with apical myosin indicated with green arrows. (**B**) Spatial profile of basal myosin intensity at T_{cell} = 9 min for wildtype (black) and *toll vl* mutant (blue) embryos. Average performed over 5 wildtype and 6 *toll vl*

mutant embryos. (**C**) Average of apical myosin over the posterior of the embryo ($-0.1 < s < 0.15$; green) and spatial average of the tangential velocity as a function of time (black) for 5 wildtype embryos. Vertical dashed line marks the onset of polarized flow. (**D**) Pole cell position (pos_{pc}) as a function of time for wildtype, *toll vl*, and *cta* embryos. Average performed over 6 wildtype, 7 *toll vl*, and 7 *cta* embryos. (**E**) Spatial average of the tangential velocity as a function of time. Average performed over 5 wildtype, 6 *toll vl*, and 5 *cta* embryos. All scale bars are 50 μm. Error bars represent the standard deviation.

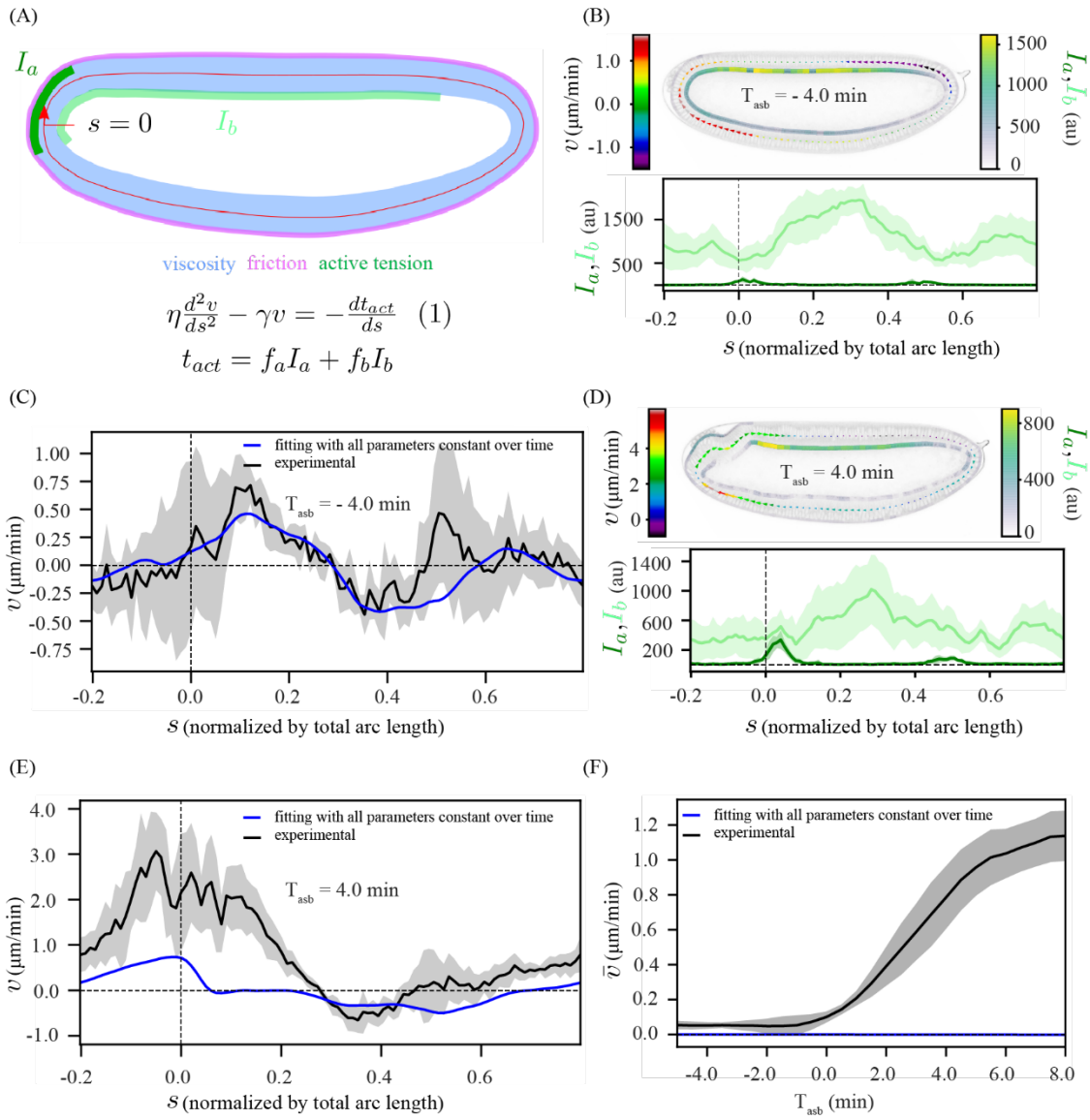

Fig. 3. A model based on an active tension mechanism explains the symmetric flow. (A) Schematic representation of our modeling framework, equation (1), in which the epithelium is considered as a viscous fluid (η, blue) with homogeneous friction (γ, pink) with the surroundings, along with domains of apical myosin (I_a, dark green) and basal myosin (I_b, light green) as contractile elements. The tissue is approximated by a 1D continuous membrane, positioned along the midline of the epithelium (red line). At any given position, s, the tangential component of the velocity (v) fulfills equation (1). **(B, D)** (*top*): a representative time frame with a heatmap of v, I_a and I_b, (*bottom*): the corresponding spatial profiles of I_a and I_b. (**B**) from the symmetric phase at T_{asb} = -4 min (**D**) from the polarized phase at T_{asb} = 4 min. **(C, E)** Simultaneous fit (blue) of equation

(1) to the experimentally measured v (black) for time points between T_{asb} = -5 min and T_{asb} = 8 min, with all parameters constant over time (see ***SI Appendix***). **(C)** T_{asb} = -4 min, **(E)** T_{asb} = 4 min. **(F)** Temporal profile of spatially averaged velocity ($\bar{v}$) in experiment (black) and from our simultaneous fit (blue). The shaded regions associated to experimental data is the standard deviation, computed over 6 embryos.

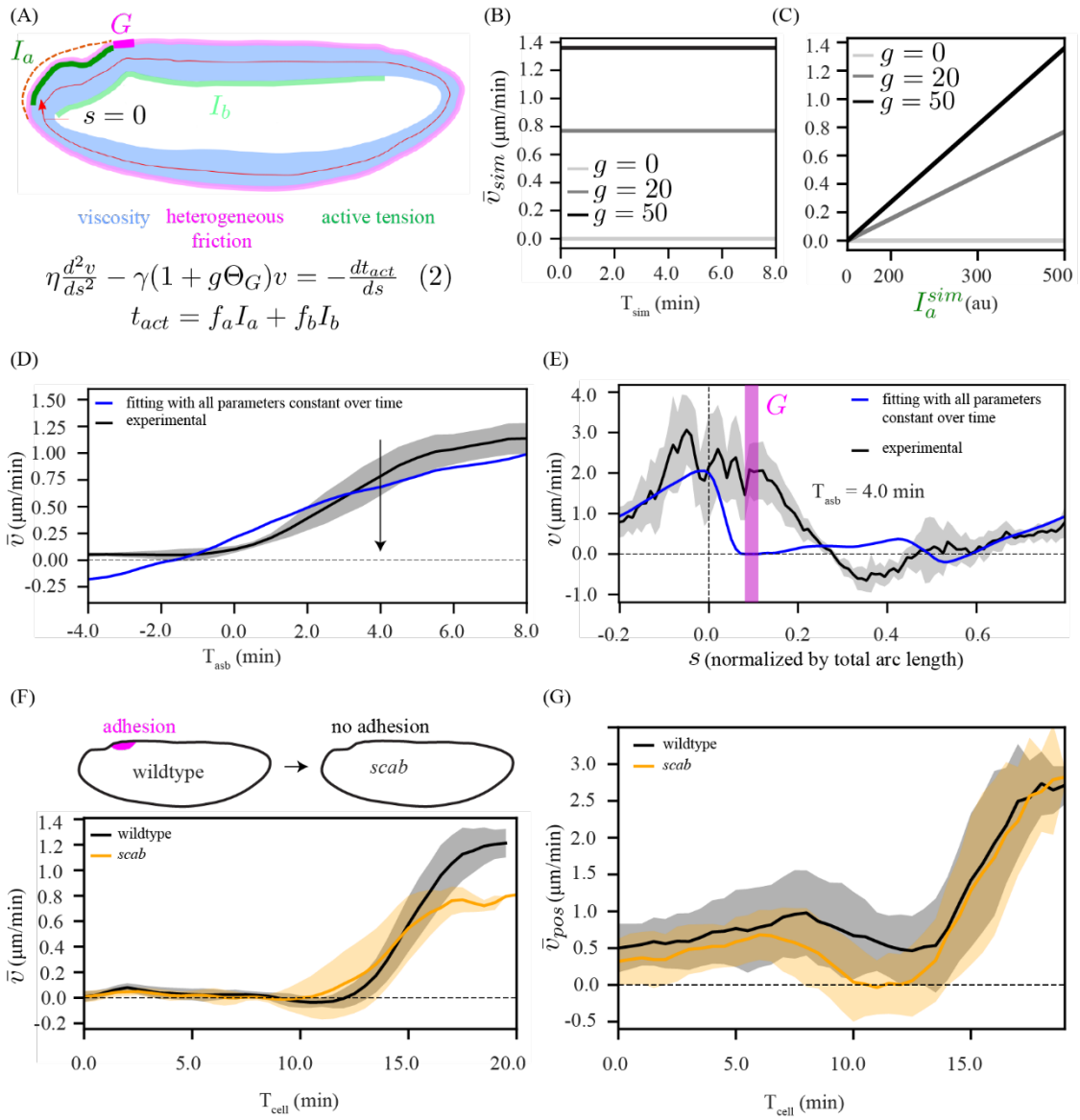

Fig. 4. Adhesion (or heterogeneous friction)-active tension coupling based model cannot explain the polarized flow. (A) Schematic representation of our model, equation (2), which is similar to equation (1) in **Fig. 3 A**, but with an additional domain *G* (magenta) of localized increase in friction by a factor *g*. **(B, C)** Elliptic model simulation (**Fig. S5 A**, **B**): **(B)** temporal profile of the spatially averaged velocity ($\bar{v}_{sim}$) when myosin intensity (I^a_{sim}) is constant over time, shown for three different values of *g*, **(C)** Dependence of $\bar{v}_{sim}$ on temporal increase in I^a_{sim}, shown for three different values of *g*. **(D)** Experimentally measured temporal profile of spatially averaged velocity $\bar{v}$ (black) and fit of equation (2) (blue), using the same procedure as described in **Fig. 3**. **(E)** Spatial fit curve corresponding to the panel **D** at a presentative time

point during the asymmetric phase (T_{asb} = 4 min**)**. **(F)** (*top*) schematic diagram of *scab* knockout, (*bottom*) temporal profile of $\bar{v}$ for wildtype (black) and *scab* (orange). **(G)** Temporal profile of spatially averaged velocity $\bar{v}_{pos}$, where average was performed only over a posterior domain from *s* = -0.1 to *s* = 0.15, for wildtype (black) and *scab* (orange). The shaded regions associated to experimental data is the standard deviation, computed over 6 embryos.

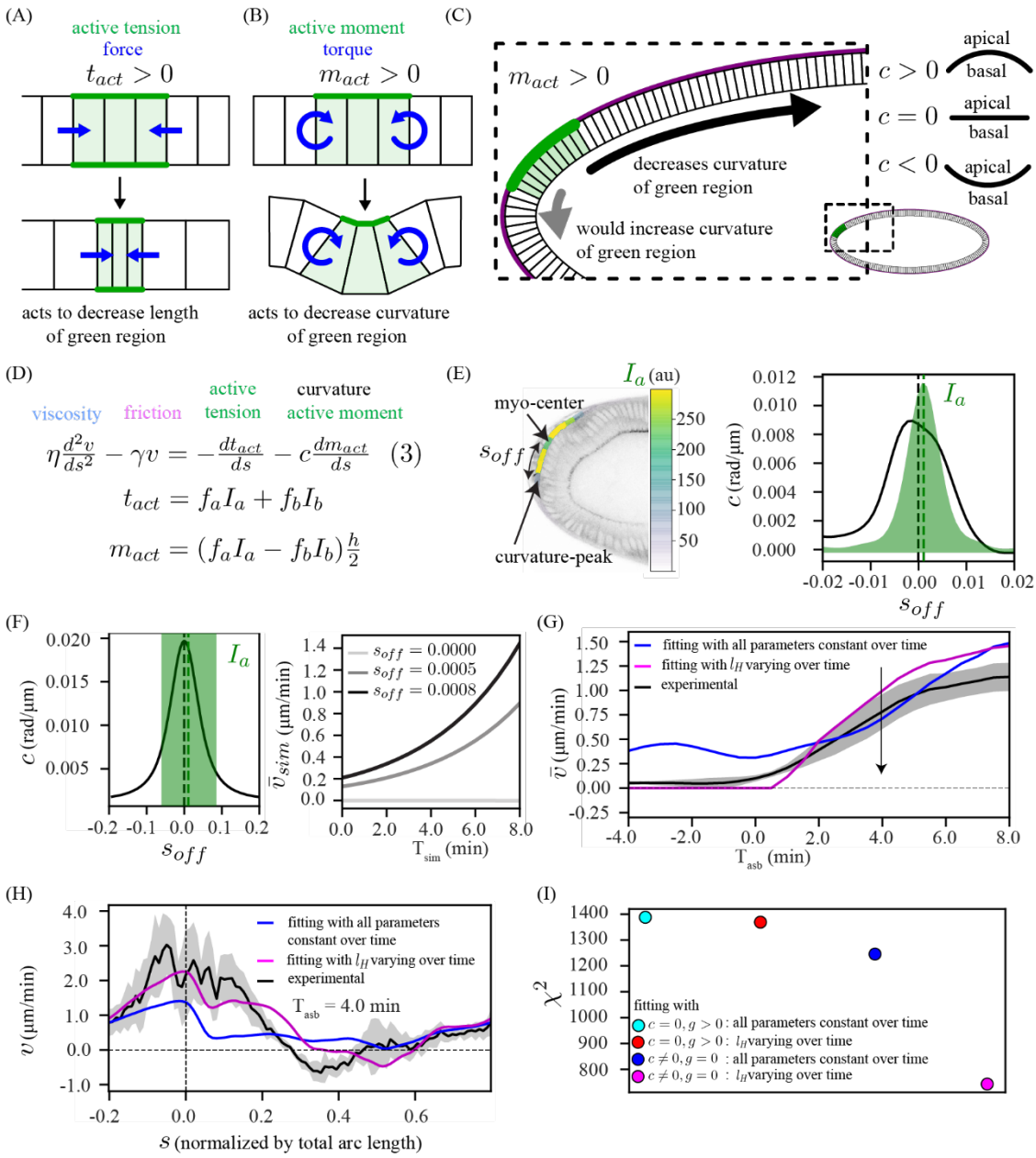

Fig. 5. A curvature-active moment coupling based model can explain the polarized flow. (A) Active tension (t_{act}, green) exerts forces (blue arrows) to contract the green region. **(B)** Active moment (m_{act}, green) exerts torques (blue arrows) to decrease curvature of the green region. **(C)** Positive active moment (m_{act} > 0) interacts with the eggshell to drive the tissue in a direction that allows the green region to decrease its curvature (black arrow), with sign convention c > 0 (convex) and c < 0 (concave). **(D)** Model equation (3): equation (1) with a curvature-active-moment coupling term. **(E)** Experimental mismatch (s_{off}) between

curvature-peak and apical myosin center. **(F**) Elliptic model simulation (**Fig. S6 A, B**): (left) illustration of s_{off}. (right) temporal profile of the spatially averaged velocity ($\bar{v}_{sim}$) with constant myosin intensity (I^{a}_{sim}), for three different values for s_{off}. **(G)** Experimental temporal profile of spatially averaged velocity $\bar{v}$ (black) and two fit (using the procedure in **Fig. 3**) curves to equation (3). (blue) all parameters constant, (magenta) all parameters but the hydrodynamic length (l_H) constant. **(H)** Spatial fit curves corresponding to the panel **G** at a representative time point during the polarized phase (T_{asb} **=** 4 min). **(I)** Chi-square values (χ^2) summed over all time points. Model with locally increased friction, all parameters constant (cyan) or only varying l_H (red). Model with curvature-active-moment, all parameters constant (blue) or only varying l_H (magenta)**.** The shaded regions associated to experimental data is the standard deviation, computed over 6 embryos.

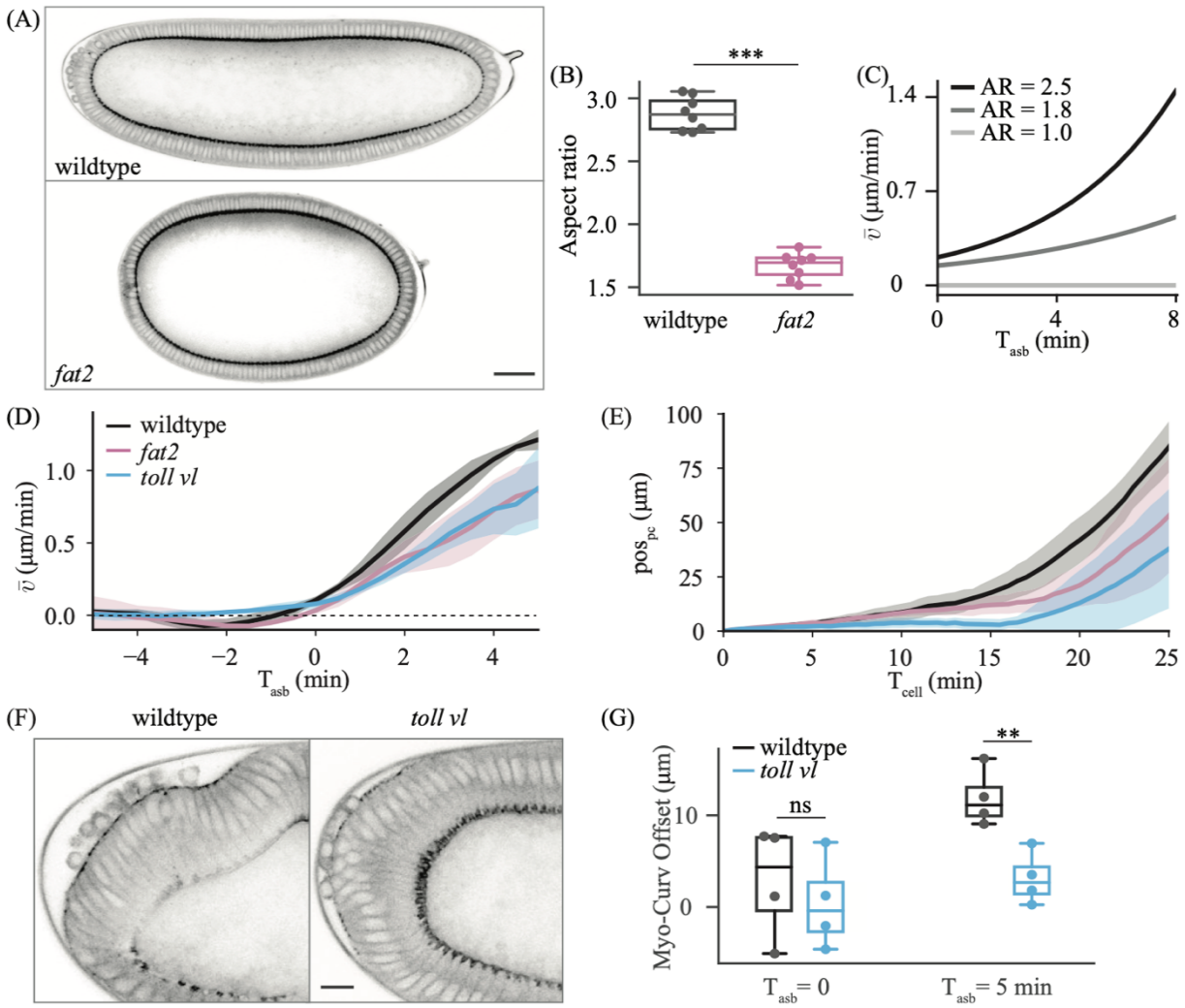

Fig. 6. Experimental perturbations to challenge model predictions. (A) Sagittal section of wildtype (top) and *fat2* (bottom) embryos at T_{cell} = 0, imaged for *sqh*::GFP. Scale bar is 50 μm. **(B)** Quantification of aspect ratio, defined as the length of the major embryo axis divided by the maximal height of the embryo for 8 wildtype and 8 *fat2* embryos. **(C)** Average velocity of tissue flow resulting from simulations using our elliptic model with different aspect ratios (AR). In the simulations (**Fig. S5 E**), the position and extent of the myosin domain was initialized consistent with the experimental data. **(D)** Experimental spatially averaged tangential velocity as a function of time after symmetry breaking for 5 wildtype, 4 *fat2*, and 6 *toll vl* embryos. **(E)** Pole cell position (pos_{pc}) as a function of time for 6 wildtype, 5 *fat 2*, and 7 *toll vl* embryos. **(F)** View of the posterior of a wildtype (left) and *toll vl* (right) embryo imaged for *sqh*::GFP. Scale bar is 10 μm. **(G)** Quantification of the offset between the position of maximum curvature and the center of the patch of posterior myosin (Myo-

1 Curv Offset) for 4 wildtype and 4 *toll vl* embryos. Comparisons in **B** and **G** performed using two-tailed

2 unpaired t-test. ns, not significant; **, $p < 0.01$; ***, $p < 0.001$.

PNAS

Supporting Information for

Curvature gradient drives polarized tissue flow in the Drosophila embryo

Emily Gehrels[1,†], Bandan Chakrabortty[1,†], Matthias Merkel[2,*] & Thomas Lecuit[1,3,*]

Corresponding authors: Matthias Merkel and Thomas Lecuit

Emails: matthias.merkel@univ-amu.fr; thomas.lecuit@univ-amu.fr

This PDF includes:

Supplementary methods
Supporting Text
Figures S1 to S9
Legends for Movies S1 to S8
SI References

Other supporting materials for this manuscript include the following:

Movies S1 to S8

Supplementary Methods

Fly lines

The following mutant alleles were used: *eve*^{3} (Bloomington stock 299), *twi*^{1} (Bloomington stock 2381), *sna*^{18} (Bloomington stock 2311), *toll*^{rm9} and *toll*^{rm10} (gift from Maria Leptin), *cta*^{RC10} (gift from Maria Leptin), *cic*^{1} (gift from Gerardo Jiménez), *traffic jam (tj)-GAL4* (*P{w[+mW.hs]=GawB}NP1624 / CyO, P{w[-]=UAS-lacZ.UW14}UW14*) (Kyoto Stock Center 104055) and *UAS-fat2 RNAi* (*P{GD14442}v27113*) (Vienna Drosophila Resource Center 27113) (gifts from Sally Horne-Badovinac), scabKO (generated in the laboratory using CRISPR by Jean-Marc Philippe), *osk-Gal4*, *UASp-CIBN-pmGFP*, and *UASp-CRY2-RhoGEF2* (gift from Stefano de Renzis). The triple mutant ;*eve*^{3}, *twist*^{1}, *snail*^{18}; used was generated in the laboratory by Claudio Collinet.

Myosin regulatory light chain (MRLC) is encoded by the gene *spaghetti squash* (*sqh*, Genebank ID: AY122159). Imaging of *sqh* was performed using *sqh-sqh::GFP* (on chromosomes 2 and 3, gift from Robert Karess). Imaging of the plasma membrane was carried out using *sqh-GAP43::mScarlet* (on chromosome 2 (9736, 2R, 53B2) and 3 (9744, 3R, 89E11) made in the laboratory by Jean-Marc Philippe). The recombinants ;*sqh-sqh::GFP,sqh-GAP43::mScarlet;* and *;;sqh-sqh::GFP,sqh-GAP43::mScarlet* were generated in the laboratory. All unique fly lines generated for this study are available from the corresponding authors upon reasonable request.

Crosses for *toll vl*: virgin *;sqh-sqh::GFP,sqh-GAP43::mSc;toll*^{rm9}*/TM6C* females were crossed with *;sqh-sqh::GFP,sqh-GAP43::mSc;toll*^{rm10}*/TM6C* males. Homozygous offspring were put in a cage.

Crosses for *fat2*: virgin ;*tj-Gal4;sqh-sqh::GFP,sqh-GAP43::mSc* females were crossed with ;*UAS-fat2 RNAi;sqh-sqh::GFP,sqh-GAP43::mSc* males. F1 virgins were crossed with ;*UAS-fat2 RNAi;sqh-sqh::GFP,sqh-GAP43::mSc* males. Resulting progeny were put in a cage.

Image Analysis

For both membrane and myosin channels, we used ImageJ software to access images of the sagittal section of the embryo from relevant time points by splitting a corresponding time series movie into individual

time frames. For extracting the apical and basal contour of the epithelium, we manually segmented a large number of frames to precisely define the respective apical and basal contours. The separation of the apical contour from the vitelline membrane is a non-trivial segmentation task, we therefore used these initially segmented frames to train a Deep Learning algorithm (namely a U-NET (46)) to do similar segmentation automatically for future movies.

To align the embryos in space**,** an ellipse (**Fig. 1 C** dashed blue ellipse) with direction of the principal axis (dashed blue line) towards the posterior side, was fitted on the apical contour of the epithelium at T_{cell} = 0 min (reference time when cellular front of epithelial cells passes the nucleus). The intersection (indicated by green star) of the principal axis with the midline (in red) of the epithelium is defined as the "zero (s = 0)" reference of the arc-length coordinate.

For myosin quantification, we developed a python script to identify the segmented apical and basal contours as closed polynomials. These polynomials were then discretized by 100 evenly spaced nodes, such that each apical node has a correspondence to the nearest basal node. For each node, a myosin-mask was defined by a quadrilateral with height approximately 10 pixels (determined by the thickness of the myosin signal) and variable width determined by the distance between the adjacent nodes. Myosin intensity at a given node was calculated by averaging the pixel intensities within the respective mask.

To extract model inputs, we constructed a midline contour by a new set of nodes defined by the average of each pair of respective apical and basal nodes. At each midline node, we computed tissue velocity via particle image velocimetry (PIV, using python library openpiv), total myosin intensity (sum of the myosin intensity at the apical and basal nodes), active-moment (product of the difference in myosin intensity at the apical and basal nodes with the distance of the midline node from either the apical or the basal node) and curvature (spatial derivative of the angle between the adjacent pair of midline edges).

Supporting Text

1 <u>Derivation of the model equation</u>

In this section we derive the model equation Eq. (3) in the main text that predicts the tangential flow in the embryo. In brief, this equation describes the embryo as an overdamped liquid (**Fig. S3A**,**3B**), which is driven by active tensions at the apical and basal surfaces of the epithelium. We use elements from the theory of active surfaces(1).

1.1 Description of the Drosophila embryo as a time-dependent 1D manifold

For simplicity, we describe the *Drosophila* embryo as a time-dependent 1D manifold $\mathbf{x}(s,T)$ that follows the epithelial midline in a mid-sagittal section of the embryo. For given position s and time T, $\mathbf{x}$ is a position in 2D euclidean space, which corresponds to the mid-saggital section when seen from the embryo's right side (as in **Fig. 1A,B** in the main text). It is parameterized by a scalar s such that the manifold is a loop and runs in clockwise sense with increasing s, such that it successively passes through dorsal, anterior, ventral, and posterior part of the embryo, respectively (as in **Fig. 1C** in the main text).

Based on the manifold $\mathbf{x}(s,T)$, we introduce for given s and T the tangent vector $\mathbf{e}$ and length e, unit normal vector pointing outside $\mathbf{n}$, and local curvature c following standard definitions:

$$\mathbf{e} = \partial_s \mathbf{x}$$

$$e = |\mathbf{e}|$$

$$\mathbf{n} = \frac{1}{e}\boldsymbol{\varepsilon}\cdot\mathbf{e} \qquad \text{S1}$$

$$c = -\frac{1}{e^2}(\partial_s \mathbf{e})\cdot\mathbf{n}$$

Here, the tensor $\boldsymbol{\varepsilon}$ is the generator of counter-clockwise rotations

$$\boldsymbol{\varepsilon} = \begin{pmatrix} 0 & -1 \\ 1 & 0 \end{pmatrix}$$

and $\cdot$ denotes the inner product.

Apical and basal surfaces of the embryo are then, respectively:

$$\mathbf{x}^{\frac{a}{b}}(s,T) \quad = \mathbf{x}(s,T) \pm \frac{h}{2}\mathbf{n}(s,T), \qquad \text{S2}$$

where the superscripts a and b correspond to apical and basal surface, and to the signs $+$ and $-$ on the right-hand side, respectively. The variable h denotes the epithelial height. The corresponding tangential vectors are:

$$\mathbf{e}^{\frac{a}{b}} = \partial_s \mathbf{x}^{\frac{a}{b}} = \left(1 \pm \frac{hc}{2}\right)\mathbf{e}. \qquad \text{S3}$$

In the second step, we inserted Eqs. S2 and used the relation $\partial_s \mathbf{n} = c\mathbf{e}$. Moreover, we ignored spatial variations in epithelial height h here (**Fig. S3C**).

1.2 Force and torque balance

To define the tension $\mathbf{t}$ at some position s of the embryo, we consider an imaginary interface at s that is orthogonal to the manifold $\mathbf{x}(s,T)$. Then, $\mathbf{t}$ is defined as the force that the part of the embryo behind this interface (larger s) exerts on the part of the embryo in front of this interface (smaller s). We denote tangential and normal components of $\mathbf{t}$ by:

$$t = \frac{1}{e}\mathbf{e} \cdot \mathbf{t}$$

$$t_n = \mathbf{n} \cdot \mathbf{t}. \qquad \text{S4}$$

Analogously, we define the moment m at position s as the torque that the portion of the embryo behind the interface at s exerts on the portion of the embryo in front of the interface. The variable m corresponds thereby to the torque component perpendicular to the mid-sagittal plane (from right to left side of the embryo). We do not consider any other torque component in our 1D model here.

We consider three kinds of external forces that are applied on the embryo: (i) a force density f^a describing friction with the vitelline membrane, which acts tangentially on the apical surface, (ii) a normal force density $-p^a$ acting on the apical surface, which corresponds to the normal force by the vitelline membrane (where the embryo touches the vitelline membrane) or the pressure in the perivitelline space (where the embryo does not touch the vitelline membrane), and (iii) a normal force density p^b that corresponds to the yolk pressure. We ignore here a tangential force on the basal surface by yolk viscosity (see Sec 3.2). Ignoring inertia, force and torque balance in terms of t, t_n, and m are then (appendix A):

$$t' + ct_n = -\left(1 + \frac{hc}{2}\right) f^a (\text{tangential force}) \tag{S5}$$

$$t_n{}' - ct = -\Delta p + \bar{p}hc (\text{normal force}) \tag{S6}$$

$$m' - t_n = -\frac{h}{2}\left(1 + \frac{hc}{2}\right) f^a (\text{torque}) \tag{S7}$$

where the prime denotes the arc-length derivative, $q' := (\partial_s q)/e$ for any q, $\Delta p = p^b - p^a$ is the pressure difference across the epithelium and $\bar{p} = (p^a + p^b)/2$ is the average pressure.

To obtain our model equation, Eq. (3) in the main text, force and torque balance need to be complemented by constitutive relations, which link embryonic tensions and moments to deformation, deformation rates, and active apical and basal tensions. To derive these, we follow a virtual work approach. This allows us to properly take active apical an basal tensions into account.

1.3 Virtual work

We consider virtual displacements $\delta\mathbf{x}(s,T)$ of the embryo from $\mathbf{x}(s,T)$ to $\mathbf{x}'(s,T) = \mathbf{x}(s,T) + \delta\mathbf{x}(s,T)$. These virtual displacements induce virtual mechanical work exerted by active apical and basal tensions δW_{act}, work by externally applied forces and torques δW_{ext}, a change of an effective bending energy δU_{bend}, and dissipated heat δW_{diss}. Without inertia, we have:

$$\delta W_{\text{act}} + \delta W_{\text{ext}} = \delta U_{\text{bend}} + \delta W_{\text{diss}}. \tag{S8}$$

We now derive expressions for each of these contributions.

1.3.1 Mechanical work by active apical and basal tensions, δW_{act}

The mechanical work by active apical and basal tensions is:

$$\delta W_{\text{act}} = -\oint t_{act}^a \frac{\delta e^a}{e^a} e^a \mathrm{d}s - \oint t_{act}^b \frac{\delta e^b}{e^b} e^b \mathrm{d}s = -\oint t_{act}^a \delta e^a \,\mathrm{d}s - \oint t_{act}^b \delta e^b \,\mathrm{d}s. \tag{S9}$$

Here, t_{act}^a and t_{act}^b are apical and basal active tensions, respectively, $\delta e^a/e^a$ and $\delta e^b/e^b$ are local strain in apical and basal surfaces, and $e^a \mathrm{d}s$ and $e^b \mathrm{d}s$ are infinitesimal apical and basal length elements. From Eqs. S3 follows:

$$\delta e^{a/b} = \left(1 \pm \frac{hc}{2}\right)\delta e \pm \frac{h}{2} e\delta c.$$

Insertion into Eq. S9 yields:

$$\delta W_{\text{act}} = -\oint \left[(t_{act} + cm_{act})\frac{\delta e}{e} + m_{act}\delta c\right] e\mathrm{d}s, \tag{S10}$$

where we introduced (total) active tension t_{act} and active moment m_{act} as:

$$t_{act} = t_{act}^{a} + t_{act}^{b} \tag{S11}$$

$$m_{act} = \frac{h}{2}(t_{act}^{a} - t_{act}^{b}). \tag{S12}$$

1.3.2 Mechanical work by external forces and torques, δW_{ext}

The external forces introduced in Sec 1.2 exert the following mechanical work on the embryo:

$$\delta W_{\text{ext}} = \oint \left[f^{a}\delta x_{t}^{a} - p^{a}\delta x_{n}^{a}\right] e^{a}\mathrm{d}s + \oint p^{b}\delta x_{n}^{b}\, e^{b}\mathrm{d}s, \tag{S13}$$

where $\delta x_{t}^{a} := \delta\mathbf{x}^{a} \cdot \mathbf{e}/e$ and $\delta x_{n}^{a/b} := \delta\mathbf{x}^{a/b} \cdot \mathbf{n}$ are tangential and normal component of the virtual displacements of apical and basal surface, respectively.

Using local force and torque balance, Eqs. S5–S7, this virtual work can also be expressed in terms of tangential tensions t and moments m only (appendix B):

$$\delta W_{\text{ext}} = \oint \left[(t + cm)\frac{\delta e}{e} + m\delta c\right] e\mathrm{d}s. \tag{S14}$$

1.3.3 Effective bending energy, U_{bend}

With an effective bending rigidity κ, the total effective bending energy of the embryo is

$$U_{\text{bend}} = \oint \frac{1}{2}\kappa c^{2}\, e\mathrm{d}s.$$

Its variation as a consequence of the virtual displacements $\delta\mathbf{x}$ is:

$$\delta U_{\text{bend}} = \oint \left[\frac{1}{2}\kappa c^{2}\frac{\delta e}{e} + \kappa c\delta c\right] e\mathrm{d}s. \tag{S15}$$

Here, we assumed that the local bending rigidity κ does not change when the tissue is strained.

1.3.4 Dissipated heat, δW_{diss}

In our model, we assume that dissipation *within the embryo* occurs only due to viscous friction in tangential direction:

$$\delta W_{\mathrm{diss}} = \oint \eta u_t \frac{\delta e}{e} e \mathrm{d}s. \tag{S16}$$

Here, η is an effective 1D tissue viscosity, and u_t is the tangential strain rate. This tangential strain rate is related to the tangential and normal velocity components v and v_n as(1):

$$u_t = \mathrm{v}' + c\mathrm{v}_n.$$

Fig. S3A,**3B** shows that the contribution by the normal motion is negligible in our case, so:

$$u_t \simeq \mathrm{v}'. \tag{S17}$$

1.4 Constitutive relations

Inserting all contributions, Eqs. S10, S16, S15 and S16 with Eq. S17, into Eq. S8 and comparing the coefficients in front of δc, we obtain:

$$m = \kappa c + m_{act}. \tag{S18}$$

Comparing the coefficients in front of δe, we obtain:

$$t + cm = \frac{1}{2}\kappa c^2 + \eta \mathrm{v}' + t_{act} + cm_{act}.$$

Inserting S18, we find:

$$t = \eta \mathrm{v}' + t_{act} - \frac{1}{2}\kappa c^2. \tag{S19}$$

The last term can be interpreted as a tendency of the tissue to leave regions with a high curvature to reduce its bending energy.

1.5 Model equation

To obtain our model equation, we combine tangential force balance, Eq. S5, with torque balance, Eq. S7:

$$t' + cm' = -\left(1 + \frac{hc}{2}\right)^2 f^a.$$

Inserting the constitutive relations for t and m, Eqs. S19 and S18, we obtain:

$$\eta \mathrm{v}'' + t'_{act} + cm'_{act} = -\left(1 + \frac{hc}{2}\right)^2 f^a. \qquad \text{S20}$$

Here, we assumed homogeneous tissue viscosity η and bending rigidity κ.

Note that using t_{act} and m_{act} from Eqs. S11 and S12 just as ad-hoc expressions for active tension and active torque in a formalism such as in(1) can lead to the wrong equation. The deeper reason for this is that the active tension in(1) corresponds to the virtual work performed by linear strain for constant curvature, which corresponds to $t_{act} + cm_{act}$ (compare Eq. S10), while t_{act} is the virtual work performed by linear strain for *zero* curvature.

We set the external force acting tangentially at the apical surface to be a simple substrate friction with the vitelline membrane:

$$f^a = -\gamma \mathrm{v}.$$

Insertion in Eq. S20 yields:

$$\eta \mathrm{v}'' + t'_{act} + cm'_{act} = \left(1 + \frac{hc}{2}\right)^2 \gamma \mathrm{v}. \qquad \text{S21}$$

The prefactor in front of the substrate friction comes from two effects that add each the same factor of $(1 + hc/2)$. First, the friction force f^a is a force per length, and it acts on the apical surface, which is by a factor of $(1 + hc/2)$ longer than the midline (see also S5). Second, since the friction force acts on the apical surface instead of the midline, it locally exerts a torque on the embryo (see also S7), which enters the tangential force balance when eliminating the normal tension t_n.

In our system, we find that hc is smaller than 1, even though it can reach ≈ 0.4 at the poles (**Fig. S3D**). However, at the poles, the epithelium is often further apart from the eggshell, without any noticeable impact on the flow. For simplicity, we thus absorb the factors $(1 + hc/2)$ on the right

hand side of Eq. S21 into a homogeneous friction coefficient γ. Rearranging the terms, we thus have:

$$\eta \mathrm{v}'' - \gamma \mathrm{v} = -t'_{act} - cm'_{act}. \qquad \text{S22}$$

This is equation (3) in the main text (in **Fig. 5D**). Equation (1) (in **Fig. 3A**) follows from leaving away the last term on the right-hand side in Eq. S22, and equation (2) (**Fig. 4A**) results from including a locally increased friction g.

2 Emergence of polarized flow

To illustrate the fundamental mechanism driving polarized flow in our model (**Fig. 5A-C** in the main text), we focus on the simplified situation where the pressure difference Δp is large enough to prevent any invagination. In other words, the embryo midline follows a time-independent curve $\mathbf{x}_{vm}(s)$ prescribed by the vitelline membrane. If we additionally assume for simplicity that the embryo is incompressible and s is an arc-length coordinate, we have:

$$\mathbf{x}(s,T) = \mathbf{x}_{vm}\big(s + s_e(T)\big).$$

In other words, the configuration of the embryo can be entirely described by the time dependence of $s_e(T)$, which describes how the embryo shifts around within the vitelline membrane.

In this case, the interaction between active moment m_{act} and curvature of the vitelline membrane creates an effective force F_{act} that tends to move the whole epithelium in clockwise direction. To see this, we note that such a force corresponds to a virtual work $\delta W_{\mathrm{act}} = F_{act}\delta s_e$. Since the embryo experiences no strain in tangential direction, the virtual mechanical work by apical and basal tensions, Eq. S10, is:

$$\delta W_{\mathrm{act}} = -\oint m_{act}(s)\delta c(s)\,\mathrm{d}s,$$

where $e = 1$ since s is arc length variable here. Using $\delta c(s) = c_{vm}{}'(s + s_e)\delta s_e$, where c_{vm} is the local curvature corresponding to $\mathbf{x}_{vm}$, we get:

$$\delta W_{\mathrm{act}} = -\delta s_e \oint m_{act}(s) c_{vm}{}'(s + s_e)\, \mathrm{d}s.$$

We thus obtain for F_{act}:

$$F_{act} = -\oint m_{act}(s) c_{vm}{}'(s + s_e)\, \mathrm{d}s.$$

Or, using a partial integration:

$$F_{act} = \oint m'_{act}(s) c_{vm}(s + s_e) \mathrm{d}s. \qquad \text{S23}$$

Note that this corresponds to the integral of the left-hand side of the tangential force balance equation, Eq. S20.

3 Orders of magnitude

3.1 Speed of polarized flow

To compute the speed of the polarized flow, we use the scenario discussed in Sec 2, i.e. the pressure is large enough for the embryo to be entirely in contact with the embryo, and the embryo is incompressible in tangential direction. Moreover, we consider here a sagittal section with lateral width Δz, centered around the mid-sagittal plane.

To obtain a rough order of magnitude for the velocity of the polarized flow, we consider an active moment profile of $m_{act}(s) = m^0_{act}$ for $s \in [s_1, s_2]$, and otherwise $m_{act}(s) = 0$. Then we obtain for the effective force F_{act} driving the polarized flow, using Eq. S23:

$$F_{act} = m^0_{act} \Delta c,$$

where $\Delta c = c_1 - c_2$ with $c_1 := c(s_1 + s_e)$ and $c_2 := c(s_2 + s_e)$. The active moment results in our system from an active tension t^0_{act} that appears apically, and with Eq. S12:

$$F_{act} = t^0_{act} \frac{h \Delta c}{2}.$$

We equate this force with a friction force $F_{ext} = \alpha \Delta z L \bar{\mathrm{v}}$ against the vitelline membrane, where L is the total length of the embryo and $\alpha = \gamma / \Delta z$ is the friction coefficient between embryo and vitelline membrane. We thus obtain for the average tangential speed $\bar{\mathrm{v}}$:

$$\bar{\mathrm{v}} = \frac{t_{act}^0}{\Delta z L \alpha} \frac{h \Delta c}{2}.$$

With $t_{act}^0 / \Delta z \sim 30$ pN · μm^{-1} (tension of myosin-enriched cell-cell interface in the embryo ~ 300 pN (2) and cell size ~ 10 μm), $L \approx 10^3$ μm, and $h \Delta c \sim 0.3$ (**Fig. S3D**), and a friction right after cellularization of $\alpha \approx 3$ pN · s · μm^{-3} (3), we obtain

$$\bar{\mathrm{v}} \sim 0.1 \text{ μm} \cdot \text{min}^{-1}.$$

This suggests that a curvature-to-active-moment coupling would be sufficient to drive the flow with average speed $\bar{\mathrm{v}} \sim 1$ μm · min^{-1} when the friction with the egg shell decreases by around an order of magnitude, consistent with our quantitative fits.

3.2 Effect of yolk viscosity

In our modeling we have neglected the yolk viscosity, because its effect can be neglected as compared to the friction of the embryo with the vitelline membrane. The friction coefficient between embryo and vitelline membrane right after cellularization has been determined to be $\alpha \approx 2 \ldots 3$ pN · s · μm^{-3} (3).

To compare this to the mechanical effect of the yolk viscosity on the embryo, we consider a situation where a velocity difference of $\Delta \mathrm{v}$ between dorsal and ventral part of the embryo create a simple shear flow with shear rate $\Delta \mathrm{v} / H$ in the yolk, where $H \approx 50$ μm is the distance between basal surfaces of dorsal and ventral parts of the embryo. This shear flow leads to a friction force density of $f_Y = \eta_Y \Delta \mathrm{v} / H$, where the yolk viscosity was measured to be $\eta_Y \approx 1$ Pa · s (4). The yolk thus exerts a friction force density of maximally $f_Y / \Delta v \approx 0.02$ pN · s · μm^{-3}. This is two orders of magnitude smaller than the friction forces between embryo and vitelline membrane right after cellularization.

4 <u>Model fitting and prediction</u>

4.1 Retrograde flow

To discuss retrograde flow, we first note that equation (2) in **Fig. 4A** of the main text results from Eq. S22 by neglecting the last term and spatially modulating friction:

$$\eta \mathrm{v}'' - (1 + g\Theta_G)\gamma \mathrm{v} = -t'_{act}, \qquad \text{S24}$$

where

$$\Theta_G(s) = \begin{cases} 1 & \text{if } s \in G \\ 0 & \text{if } s \notin G \end{cases}$$

with G being a small region posterior to the apical myosin patch.

Formally, the existence of retrograde flow and its magnitude follows from integrating Eq. S24 over the whole domain of the embryo:

$$\bar{\mathrm{v}} = -\frac{g\ell_G}{L}\bar{\mathrm{v}}_G. \qquad \text{S25}$$

Here, $\bar{\mathrm{v}}$ is the tangential velocity averaged over the whole epithelium, L is the length of the whole epithelium, ℓ_G is the length of region G, and $\bar{\mathrm{v}}_G$ is the tangential velocity averaged over region G. From Eq. S25 with $g > 0$ follows directly that overall average flow $\bar{\mathrm{v}}$ and $\bar{\mathrm{v}}_G$ have opposite sign, implying retrorade flow within G.This is because frictional force in the high friction ($g > 0$) region must be balanced by frictional force in the other, low friction ($g = 0$) region. Since frictional force is proportional to velocity and total force must sum to zero, this means that if the velocity in the low friction region is positive (clockwise), the velocity in the region of high friction will have to be negative (counterclockwise). Moreover, the absence of localized friction, $g = 0$, implies zero average velocity, $\bar{\mathrm{v}} = 0$.

4.2 Model Fitting

To quantitatively compare equations (1)–(3) in the main text (which follow from Eq. S22) to experimental data, we assumed a linear relation between apical and basal active tension, t^a_{act} and t^b_{act}, and the respective sqh::GFP signal, I_a and I_b:

$$t^a_{act} = f_a I_a \quad t^b_{act} = f_b I_b.$$

We assume that f_a and f_b can be different, where due to the different cytoskeletal structures apically and basally, we expect $f_a > f_b$. According to Eqs. S11 and S12, we thus have:

$$\begin{aligned} t_{act} &= f_a I_a + f_b I_b \\ m_{act} &= (f_a I_a - f_b I_b)\frac{h}{2}. \end{aligned}$$

Insertion into equation (3) in the main text (i.e. Eq. S22) and division by η yields:

$$\mathrm{v}'' - \frac{1}{l_H^2}\mathrm{v} = -r_a I_a'\left(1 + \frac{ch}{2}\right) - r_b I_b'\left(1 - \frac{ch}{2}\right), \qquad \text{S26}$$

where $l_H = \sqrt{\eta/\gamma}$ is the hydrodynamic length scale, $r_a = f_a/\eta$, and $r_b = f_b/\eta$. The parameters r_a and r_b have units of rates per pixel intensity – they indicate how fast the epithelium contracts per pixel intensity of myosin.

We use Eq. S26 to fit model equation (3), while using the correspondingly modified equations to fit equations (1) and (2) in the main text. In particular, we leave out the terms $\sim hc$ on the right-hand side for equations (1) and (2), and we introduce a localized friction for equation (2).

To fit to experimental data, we first use the measured c, I_a,I_b and h to numerically solve Eq. S26 for v at each time step. For this, we discretize this equation in space with regular lattice spacing $\Delta s = 0.01$ and solve the resulting linear equation in $\mathrm{v}(s)$ in python using a sparse matrix inverter.

To obtain the parameters l_H, r_a, and r_b (and g for equation (2)), we always fitted the the theoretical predictions for $\mathrm{v}(s)$ to its respective measured curves $\mathrm{v}(s)$ *at all time points simultaneously* between $T_{asb} = -5 \ldots 8$ min. To this end, we used the python routine curve-fit to minimize the squared distances between theoretical and measured v summed over all positions and times (minimal χ^2 plotted in **Fig. 5I**). In particular, we carried out two kinds of simultaneous fits. First, for many fits, we imposed that all parameter values should be the same at all time points. These corresponds to the blue curves in **Fig. 3C,E**, **4D**,**E**, and **5G**,**H**. Second, for some fits, we allowed l_H to be different for each time point, while we imposed that all other parameters have to be the same value at each time point. This corresponds to the magenta curves in **Fig. 5G**,**H** and all the fit curves in **Fig. S6D-E and** ,**Fig. S7B-F**.

4.3 Limitation on compression of apical myosin patch

We realized that our fitting of model equation (3) resulted in a substantial increase of the hydrodynamic length scale of over an order of magnitude around the time of symmetry breaking (**Fig. S6D**). Upon close examination of possible causes for this jump, we first noted that assuming a dominant role of apical myosin during the asymmetric phase, the velocity of polarized flow should scale as $\bar{v} \sim f_a I_a/\gamma = I_a r_a l_H^2$. Second, we noticed a steep decrease in velocity in our velocity fit curves in the region where the apical myosin patch is, around $s \approx 0.03$ (magenta curves in **Fig. 5H**, blue region in **Fig. S6E**). This velocity decrease in the fit curves corresponds to a strong contractile flow, which is created by apical myosin and resisted by tissue viscosity. The corresponding contraction rate is of order $\sim f_a I_a/\eta = I_a r_a$. Taken together, in our χ^2 minimization-based fitting, to keep the contraction of the apical myosin patch close to measured values while keeping large enough $\bar{v}$, the hydrodynamic length scale l_H needs to be large during the asymmetric phase.

To test these ideas, we also examined a model where the contraction rate of the region with the apical myosin patch (the primordium) would be limited. Limiting this contraction rate makes sense, because the primordium undergoes isotropic contraction. Indeed, this region around the apical myosin distribution has increased epithelial height in the asymmetric phase (**Fig. S6F**). There will thus be a limit on how far this part of the tissue will be able to contract until elastic resistance prevents further contraction. In our model, we do not have included elasticity, which would require including an additional parameter and defining reference states. To circumvent these issues and keep the model simple, we have decided to study the consequences of a limited primordium contraction rate in a symmetric region around the peak of apical myosin distribution at $s = 0.03$ (**Fig. S6F**) by substantially increasing viscosity in the primordium region (Eq. 4 in **Fig. 7SA**).

We show results of fits where we locally increased viscosity by a factor of $e = 100^{**}$ with varying length $0.08 \geq L_E \geq 0.0$, i.e restricting within the apical myosin domain. We find that the contraction rate in the primordium region is indeed decreased (**Fig. S7B**). Moreover, the corresponding increase in hydrodynamic length scale is also much smaller now, from $l_H \approx 0.04$ $(40\ \mu m)$ during symmetric flow to $l_H \approx 0.4$ $(400\ \mu m)$during asymmetric flow (**Fig. S7C**). Taken together, taking into account a limited primordium

contraction rate, our data can be explained better (smaller χ^2, see **Fig. S7D**) and with a smaller decrease in friction with the eggshell.

We find that our results are largely independent of the increase in viscosity as long as $e > 10$ (Fig. S7E**, **F**).

4.4 Simulations using a simplified model

To obtain a better intuition, we simplified the embryo by representing its shape as an ellipse (elliptic contour in **Fig. S5A**,**6A**), discretized by 100 evenly spaced nodes. For these simulations we neglected basal myosin and approximated the distribution of apical myosin by a rectangular function (green patch in **Fig. S5B,6B**) with height I_a^{sim}. To simulate equation (2), we moreover approximated the patch of increased friction, Θ_G, by another rectangular function (magenta patch in **Fig. S5B**) that advected with the epithelium. In all simulations, we choose I_a^{sim} to be of the order of experimentally measured apical myosin intensity I_a (as in **Fig. 3B**,**D**) and the values of the physical parameters were chosen from the fit values to the experimental data.

We then simulated discrete time steps $\Delta t = 0.5$ min, where at a given time point T_{sim}, we solved equation (2) or (3) for velocity using the python solver described in the previous section to obtain the velocity field $\mathrm{v}_{sim}(s)$. To further simplify our simulation, we did not allow for any deformation of the epithelium. We thus advanced the whole epithelium at each time step by the distance $\bar{\mathrm{v}}\Delta t$. This introduced a time dependence in our solution for equation (3), due to a changing offset between curvature $c(s)$ and myosin profile $I_a^{sim}(s)$.

Appendix

A. Force and torque balance

To derive the force and torque balance relations, Eqs. S5–S7, we roughly follow the approach from(1).

We start from noting that in an overdamped system, the total force acting on any piece of the embryo between s_1 and s_2 needs to vanish:

$$0 = \mathbf{t}(s_2) - \mathbf{t}(s_1) + \int_{s_1}^{s_2} \left[f^a \frac{1}{e^a} \mathbf{e}^a - p^a \mathbf{n}^a \right] e^a \mathrm{d}s + \int_{s_1}^{s_2} p^b \mathbf{n}^b \, e^b \mathrm{d}s \qquad \text{A1}$$

Here, the terms on the right hand side are the force exerted by the region of the part of embryo behind s_2, the force exerted by the part of the embryo before s_1, the external force exerted on the apical surface, and the external force exerted on the basal surface.

The derivative of Eq. A1 with respect to $s \equiv s_2$ is:

$$0 = \partial_s \mathbf{t} + f^a \mathbf{e}^a + (p^b e^b - p^a e^a)\mathbf{n} \qquad \text{A2}$$

Using Eqs. S3 and the arc-length derivative, $q' := (\partial_s q)/e$ for any q:

$$0 \quad = \mathbf{t}' + f^a \left(1 + \frac{hc}{2}\right)\frac{1}{e}\mathbf{e} + (\Delta p - \bar{p}hc)\mathbf{n}. \qquad \text{A3}$$

Here, we have defined $\Delta p = p^b - p^a$ and $\bar{p} = (p^a + p^b)/2$. Using $\mathbf{t} = t\mathbf{e}/e + t_n\mathbf{n}$ together with the relations $\mathbf{n}' = c\mathbf{e}/e$ and $(\mathbf{e}/e)' = -c\mathbf{n}$, Eq. A3 becomes:

$$\begin{aligned} 0 \quad &= t'\frac{1}{e}\mathbf{e} - ct\mathbf{n} + t_n{}'\mathbf{n} + ct_n\frac{1}{e}\mathbf{e} \\ &\quad + f^a\left(1 + \frac{hc}{2}\right)\frac{1}{e}\mathbf{e} + (\Delta p - \bar{p}hc)\mathbf{n}. \end{aligned}$$

Tangential and normal force balance, Eqs. S5 and Eq. S6, can now be directly read off directly from tangential and normal part of this equation.

The total torque acting on the same piece of embryo also needs to vanish:

$$\begin{aligned} 0 \quad &= m(s_2) + \mathbf{x}(s_2)\cdot\boldsymbol{\varepsilon}\cdot\mathbf{t}(s_2) \\ &\quad - m(s_1) - \mathbf{x}(s_1)\cdot\boldsymbol{\varepsilon}\cdot\mathbf{t}(s_1) \\ &\quad + \int_{s_1}^{s_2} \mathbf{x}^a\cdot\boldsymbol{\varepsilon}\cdot\left[f^a\frac{1}{e^a}\mathbf{e}^a - p^a\mathbf{n}^a\right] e^a \mathrm{d}s \\ &\quad + \int_{s_1}^{s_2} \mathbf{x}^b\cdot\boldsymbol{\varepsilon}\cdot p^b\mathbf{n}^b\, e^b \mathrm{d}s \end{aligned}$$

The derivative with respect to $s \equiv s_2$ is:

$$\begin{aligned} 0 \quad &= \partial_s m + \mathbf{e}\cdot\boldsymbol{\varepsilon}\cdot\mathbf{t} + \mathbf{x}\cdot\boldsymbol{\varepsilon}\cdot(\partial_s\mathbf{t}) \\ &\quad + \mathbf{x}^a\cdot\boldsymbol{\varepsilon}\cdot[f^a\mathbf{e} - p^a e^a\mathbf{n}] \\ &\quad + \mathbf{x}^b\cdot\boldsymbol{\varepsilon}\cdot p^b e^b\mathbf{n}. \end{aligned}$$

After using Eqs. S1 and S4 as well as consecutive insertion of Eqs. S2 and A2:

$$0 \quad = \partial_s m - e t_n + \frac{h}{2} f^a \mathbf{n} \cdot \boldsymbol{\varepsilon} \cdot \mathbf{e}^a$$

Insertion of Eq. S3 yields torque balance, Eq. S7:

$$0 = m' - t_n + \frac{h}{2}\left(1 + \frac{hc}{2}\right) f^a.$$

B. Virtual work by external forces and torques

Using force and torque balance, we show here that the expressions in Eqs. S13 and S14 for the virtual work by external forces and torques are equivalent(1). To this end, we start with expression Eq. S14:

$$\delta W_{\text{ext}} = \oint \left[(t + cm)\frac{\delta e}{e} + m\delta c\right] e \mathrm{d}s. \qquad \text{B1}$$

Using

$$\begin{aligned} \delta e \quad &= \frac{1}{e}\mathbf{e} \cdot \partial_s \delta \mathbf{x} \\ \delta c \quad &= -\frac{2c}{e^2}\mathbf{e} \cdot \partial_s \delta \mathbf{x} - \frac{1}{e}\mathbf{n} \cdot \partial_s \left(\frac{1}{e}\partial_s \delta \mathbf{x}\right), \end{aligned}$$

Eq. B1 becomes:

$$\begin{aligned} \delta W_{\text{ext}} \quad &= \oint (t - cm)\frac{1}{e}\mathbf{e} \cdot \partial_s \delta \mathbf{x}\, \mathrm{d}s \\ &\quad - \oint m\mathbf{n} \cdot \partial_s \left(\frac{1}{e}\partial_s \delta \mathbf{x}\right) \mathrm{d}s. \end{aligned}$$

After partial integrations:

$$\begin{aligned} \delta W_{\text{ext}} \quad &= -\oint \left(\partial_s \left[(t - cm)\frac{1}{e}\mathbf{e}\right]\right) \cdot \delta \mathbf{x}\, \mathrm{d}s \\ &\quad - \oint \left(\partial_s \left[\frac{1}{e}\partial_s [m\mathbf{n}]\right]\right) \cdot \delta \mathbf{x}\, \mathrm{d}s. \end{aligned}$$

Using $\mathbf{n}' = c\mathbf{e}/e$:

$$\delta W_{\text{ext}} \quad = -\oint \left(t\frac{1}{e}\mathbf{e} + m'\mathbf{n}\right)' \cdot \delta \mathbf{x}\, e \mathrm{d}s.$$

Using both $\mathbf{n}' = c\mathbf{e}/e$ and $(\mathbf{e}/e)' = -c\mathbf{n}$:

$$\delta W_{\text{ext}} = -\oint \left(t' \frac{1}{e}\mathbf{e} - ct\mathbf{n} + m''\mathbf{n} + cm' \frac{1}{e}\mathbf{e} \right) \cdot \delta\mathbf{x}\, e\mathrm{d}s. \tag{B2}$$

Combining tangential and normal force balance respectively with torque balance, Eqs. S5–S7, we have:

$$\begin{aligned} t' + cm' &= -\left(1 + \frac{hc}{2}\right)^2 f^a \\ m'' - ct &= -\left[\frac{h}{2}\left(1 + \frac{hc}{2}\right) f^a\right]' - \Delta p + \bar{p}hc. \end{aligned}$$

Insertion in B2 yields:

$$\begin{aligned} \delta W_{\text{ext}} &= \oint \left(1 + \frac{hc}{2}\right)^2 f^a \frac{1}{e}\mathbf{e} \cdot \delta\mathbf{x}\, e\mathrm{d}s \\ &+ \oint \left(\partial_s \left[\frac{h}{2}\left(1 + \frac{hc}{2}\right) f^a\right]\right) \mathbf{n} \cdot \delta\mathbf{x}\, \mathrm{d}s \\ &+ \oint (\Delta p - \bar{p}hc)\mathbf{n} \cdot \delta\mathbf{x}\, e\mathrm{d}s. \end{aligned}$$

After partial integration of the second integral:

$$\begin{aligned} \delta W_{\text{ext}} &= \oint \left(1 + \frac{hc}{2}\right)^2 f^a \frac{1}{e}\mathbf{e} \cdot \delta\mathbf{x}\, e\mathrm{d}s \\ &- \oint \frac{h}{2}\left(1 + \frac{hc}{2}\right) f^a (\mathbf{n} \cdot \delta\mathbf{x})'\, e\mathrm{d}s \\ &+ \oint \left(1 - \frac{hc}{2}\right) p^b \mathbf{n} \cdot \delta\mathbf{x}\, e\mathrm{d}s \\ &- \oint \left(1 + \frac{hc}{2}\right) p^a \mathbf{n} \cdot \delta\mathbf{x}\, e\mathrm{d}s. \end{aligned}$$

Using $(\mathbf{n} \cdot \delta\mathbf{x})' = c(\mathbf{e}/e) \cdot \delta\mathbf{x} + \mathbf{n} \cdot \delta\mathbf{x}'$ and $(\mathbf{e}/e) \cdot \delta\mathbf{n} = -\mathbf{n} \cdot \delta\mathbf{x}'$, as well as $\mathbf{n} \cdot \delta\mathbf{n} = 0$, this becomes:

$$\begin{aligned} \delta W_{\text{ext}} &= \oint \left(1 + \frac{hc}{2}\right) f^a \frac{1}{e}\mathbf{e} \cdot \left(\delta\mathbf{x} + \frac{h}{2}\delta\mathbf{n}\right) e\mathrm{d}s \\ &+ \oint \left(1 - \frac{hc}{2}\right) p^b \mathbf{n} \cdot \left(\delta\mathbf{x} - \frac{h}{2}\delta\mathbf{n}\right) e\mathrm{d}s \\ &- \oint \left(1 + \frac{hc}{2}\right) p^a \mathbf{n} \cdot \left(\delta\mathbf{x} + \frac{h}{2}\delta\mathbf{n}\right) e\mathrm{d}s. \end{aligned}$$

Using Eqs. S2 and S3, as well as $\mathbf{n} \cdot \delta\mathbf{n} = 0$:

$$\begin{aligned} \delta W_{\text{ext}} &= \oint f^a \frac{1}{e^a}\mathbf{e}^a \cdot \delta\mathbf{x}^a\, e^a \mathrm{d}s \\ &+ \oint p^b \mathbf{n} \cdot \delta\mathbf{x}^b\, e^b \mathrm{d}s \\ &- \oint p^a \mathbf{n} \cdot \delta\mathbf{x}^a\, e^a \mathrm{d}s. \end{aligned}$$

This is the same expression as in Eq. S13.

1 **Figures S1 to S9:**

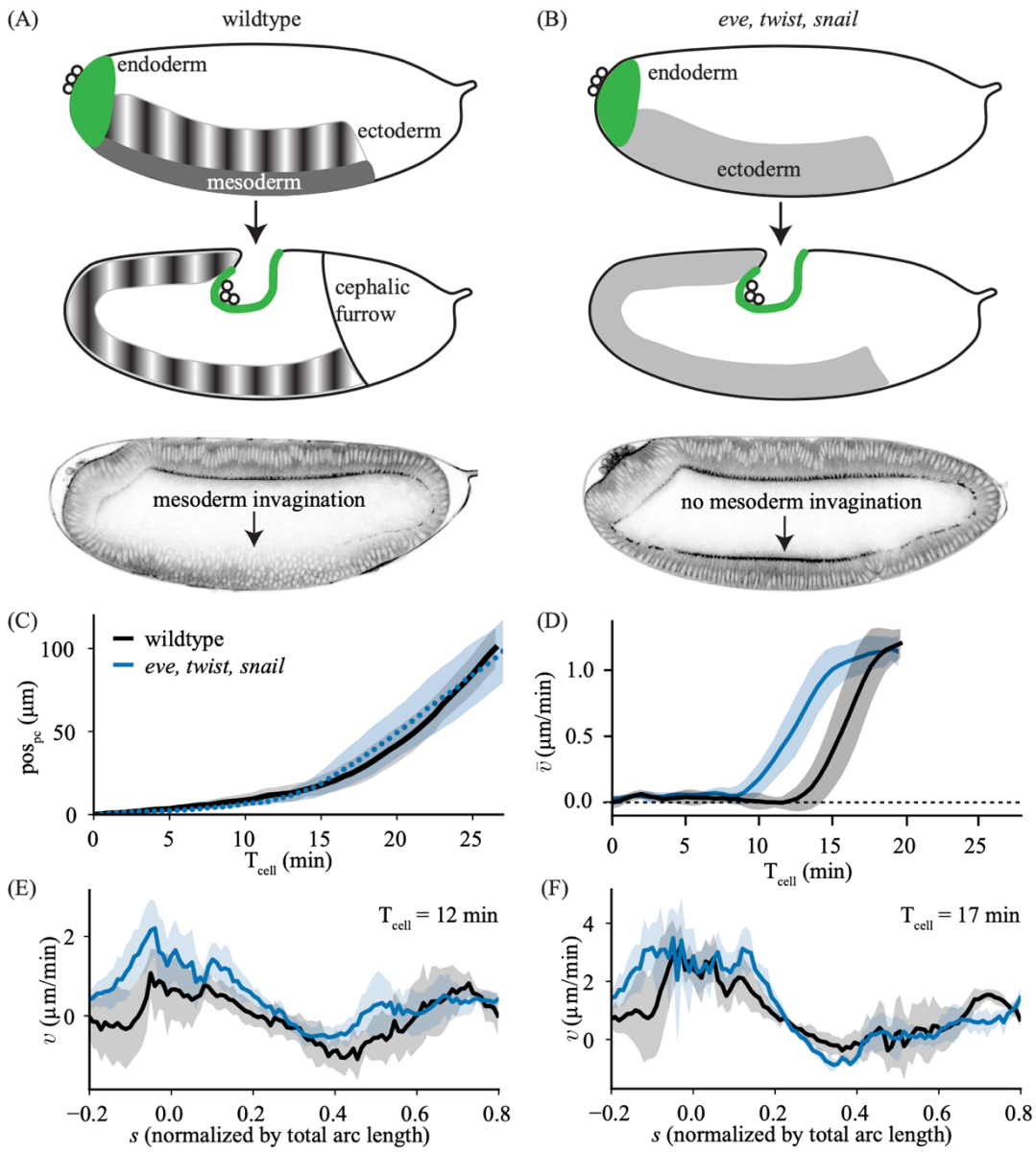

2

3 **Fig. S1. Comparison of wildtype with *eve, twist, snail* mutant embryos. (A, B)** Cartoons of *Drosophila*
4 embryo (*top*) at an early stage, during the process of cellularization and (*middle*) approximately 30 minutes
5 later for a (**A**) wildtype and (**B**) *eve, twist, snail* (*ets*) mutant embryo. This shows that in *ets* mutants the
6 mesoderm is no longer specified, there is no planar polarization of myosin in the ectoderm, and there is no
7 formation of the cephalic furrow. (*bottom*) Images of these embryos at T_{cell} = 19 min. (**C**) Quantification of
8 the position of the pole cells (pos_{pc}) as a function of time since the cellularization front passes the nuclei in

the dorsal posterior (T_{cell}). Average performed over 6 wildtype and 7 *ets* embryos. (**D**) Spatial average of the tangential velocity ($\bar{v}$) as a function of time. Average performed over 5 wildtype and 6 *ets* embryos. (**E, F**) Spatial profile of tangential velocity for wildtype and *ets* embryos at (**E**) T_{cell} = 12 min and (**F**) T_{cell} = 17 min. Error bars represent standard deviation.

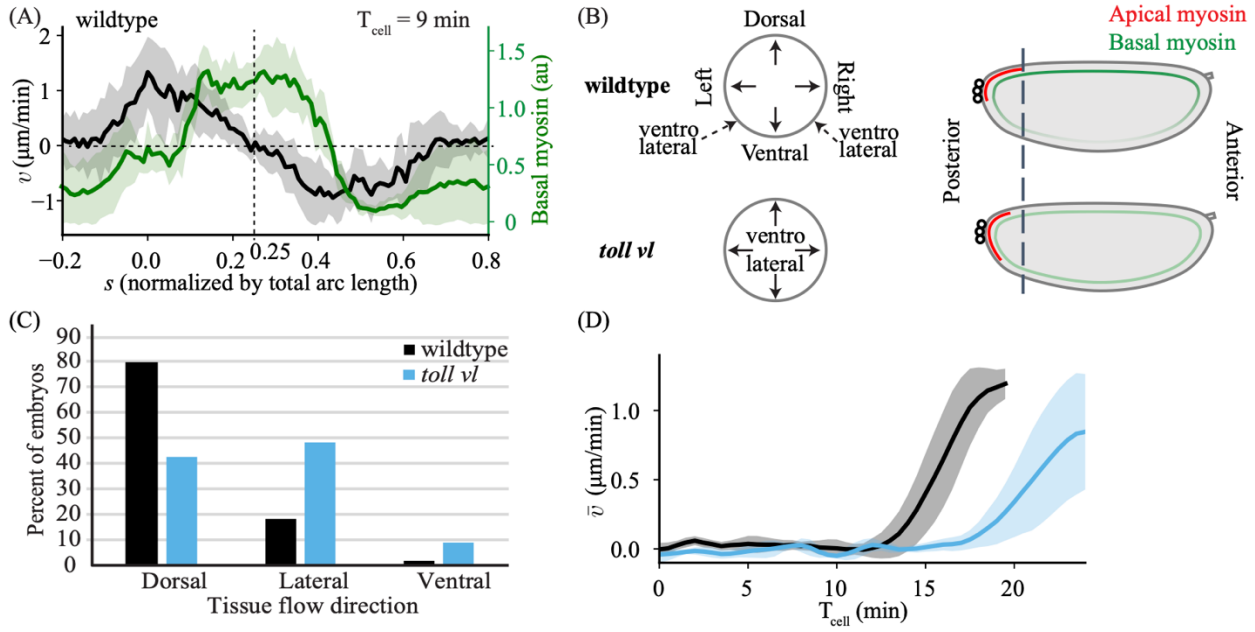

Fig. S2. Characterization of *toll vl* embryos. (**A**) Spatial profile of tangential velocity (v) and basal myosin intensity for wildtype embryos at T_{cell} = 9 min. Vertical dashed line represents the center of the dorsal side of the embryo (s = 0.25). (**B**) Schema of the difference between wildtype and *toll vl* mutant embryos shown in (*left*) a cross section along the anterior-posterior axis and (*right*) in a sagittal plane. (**C**) Quantification of the direction of tissue flow in wildtype and *toll vl* mutant embryos. Dorsal and ventral indicate that the tissue flows in the imaging plane either towards the dorsal or ventral side and lateral refers to any embryo where the tissue flow occurred out of plan. See **Movie S4** for examples of each. Data was collected on a DIC microscope for 58 wildtype embryos and 68 *toll vl* mutant embryos (see **Materials and Methods**). A Fisher's exact test was used to compare dorsal vs non-dorsal flow outcomes between wildtype and *toll vl* conditions yielding a p-value < 0.0001. (**D**) Spatial average of the tangential velocity ($\bar{v}$) as a function of time for wildtype and *toll vl* embryos as in **Fig. 2E**, but including later times. Error bars represent the standard deviation.

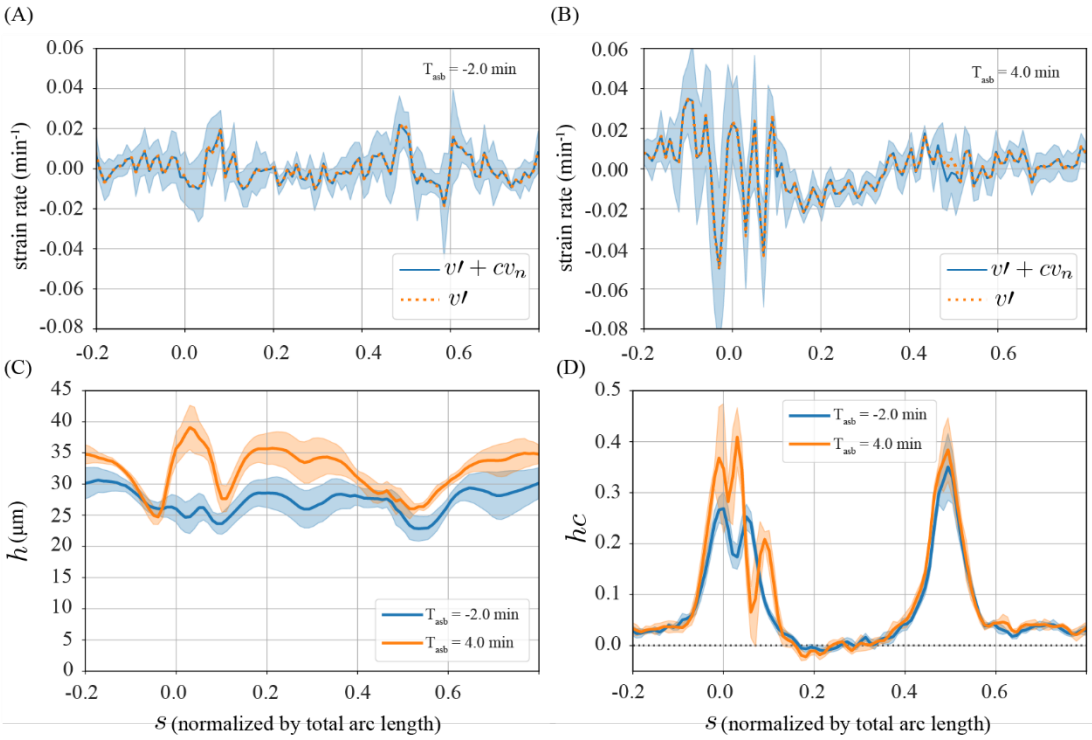

Fig. S3. Orders of magnitude in the experimental data. Data from *eve, twist, snail* mutants, which behave similar to wildtype at early times, but which does not show mesoderm invagination, so the height *h* can be measured more accurately. **(A,B)** The local strain rate (blue solid curve) is virtually identical with the derivative of the tangential velocity v' (orange dashed curve) both at **(A)** T_{asb} = -2 min and **(B)** T_{asb} = 4 min. Thus, the contribution by the normal motion of the epithelium, v_n is negligible. **(C)** The fluctuations in epithelial height (*h*) are on the order of 10% (spatial coefficient of variation). **(D)** The product *hc* is larger at the poles of the embryo, where it maximally becomes approximately 0.4. In all panels, the shaded regions indicate the standard error of the mean, computed over 6 embryos.

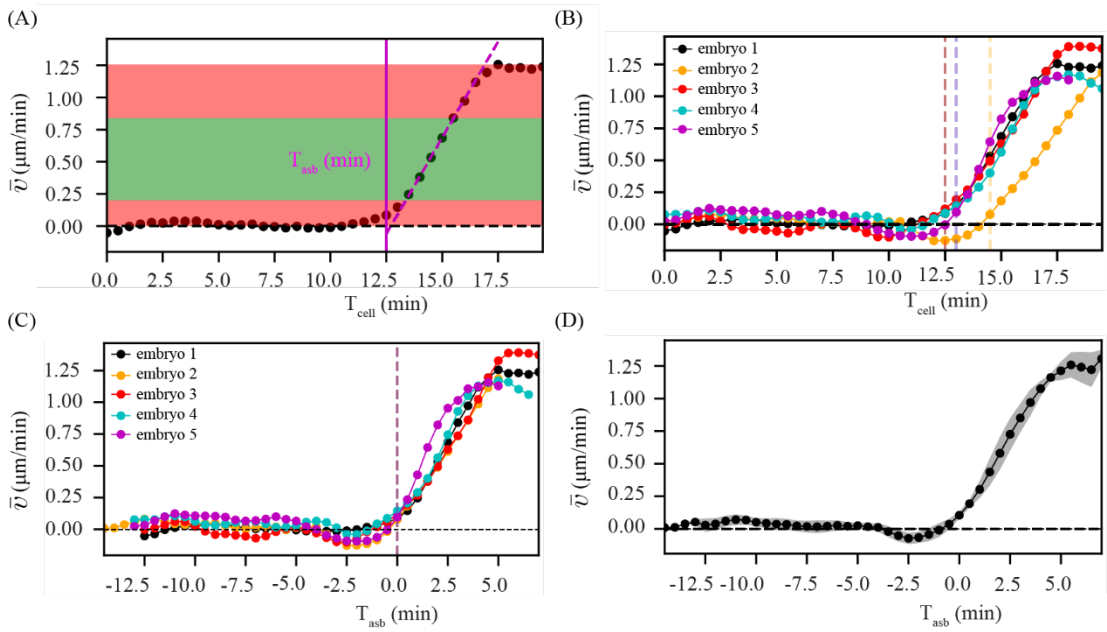

Fig. S4. Detection of symmetric to polarized transition in flow. (A) Temporal profile of the spatially averaged velocity $\bar{v}$ (black dotted curve) computed from the velocity field of individual time frames. A line is fitted in the green region ($\bar{v}$> 0.2 μm/min and the next five time points) to get an intercept with the time axis (T_{cell}). This time of intercept becomes the time of symmetry breaking T_{asb} = 0 (vertical magenta line) and used to align different embryos. **(B)** Temporal profile of $\bar{v}$ with detection of T_{asb} for many embryos, using the method described in **A**. **(C)** Temporal profile of $\bar{v}$ with rescaled time axis, where T_{asb} of the respective embryos is defined as zero reference, i.e T_{asb} < 0 min correspond to symmetric phase of flow and T_{asb} > 0 corresponds to polarized phase of flow. **(D)** Temporal profile of $\bar{v}$, now averaged over all the embryos shown in **C**. The shaded region indicates the standard deviation, computed over 5 embryos.

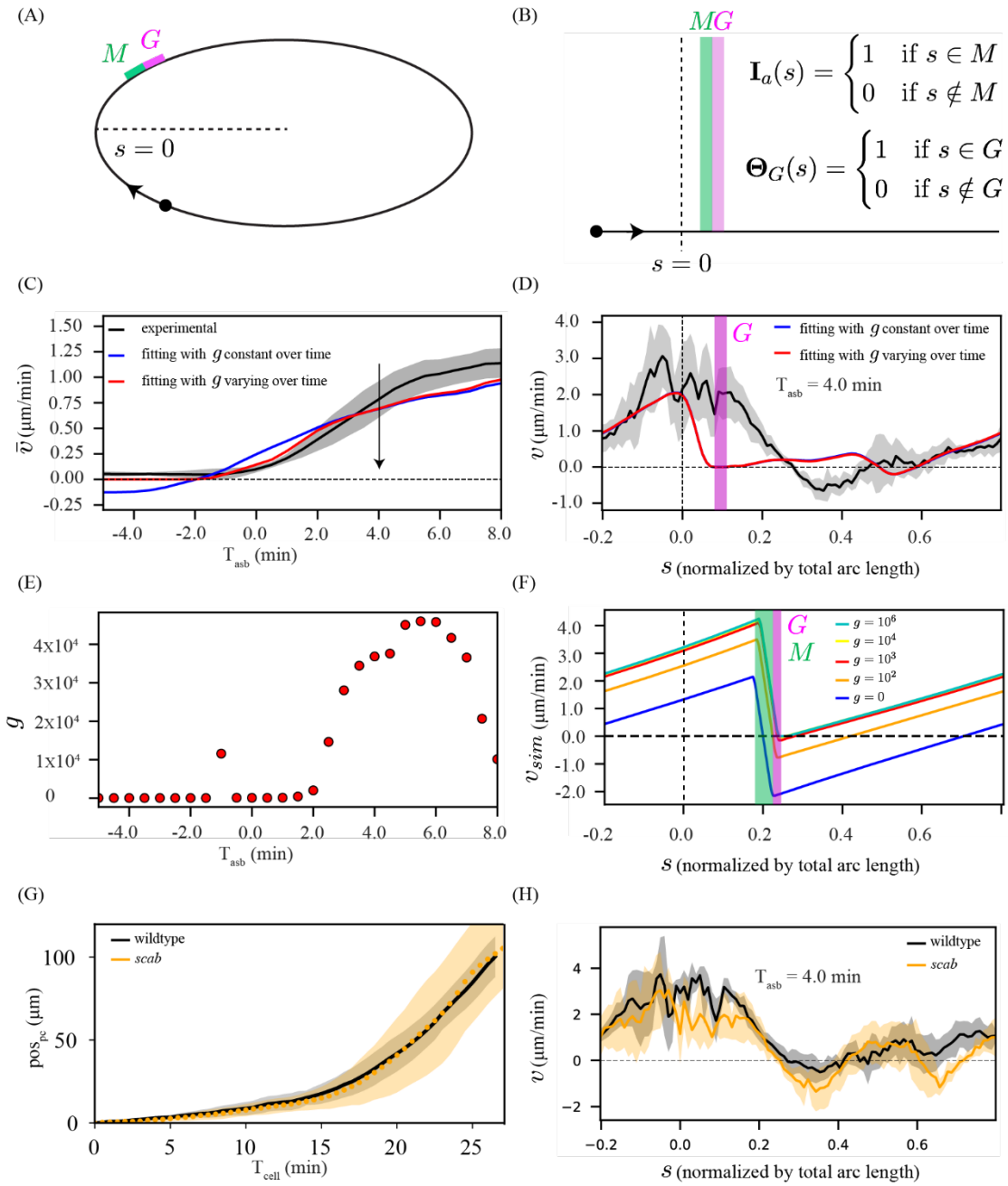

Fig. S5. Fitting with heterogeneous friction. (A) Schematic of the elliptic representation of the embryo. Green region corresponds to domain of myosin (M) and magenta region corresponds to domain of high friction (G). **(B)** 1D flat representation of **A**, where the domains M and G are mathematically described by rectangular functions. **(C)** Experimentally measured temporal profile of spatially averaged velocity $\bar{v}$ (black) and result of two fits (using the procedure described in **Fig. 3**) of equation (2): (blue) all parameters constant

and (red) all parameters but *g* constant over time. **(D)** Spatial fit curves for velocity (v), corresponding to the fits in panel **C** for a representative time point during the polarized phase **(**T_{asb} **=** 4 min). **(E)** Temporal profile of *g* corresponding to the red curves in panel **C** and **D**. **(F)** Elliptic model simulation: spatial profile of velocity (v_{sim}) by simulating equation (2) when myosin intensity (I^{a}_{sim}) is constant over time, shown for five different values of *g*. These simulations indicate retrograde (counterclockwise) flow in the region of high friction *G*. (**G**) Quantification of the pole cell position (pos_{pc}, see **Materials and Methods**) as a function of T_{cell}. Average performed over 6 wildtype (black) and 6 *scab* (orange) embryos. (**H**) Experimentally measured spatial velocity profile (v) in wildtype (black) and *scab* embryos (orange) at a representative time point T_{asb} = 4 min. Average performed over 5 wildtype and 5 *scab* embryos. The shaded regions associated to experimental data is the standard deviation.

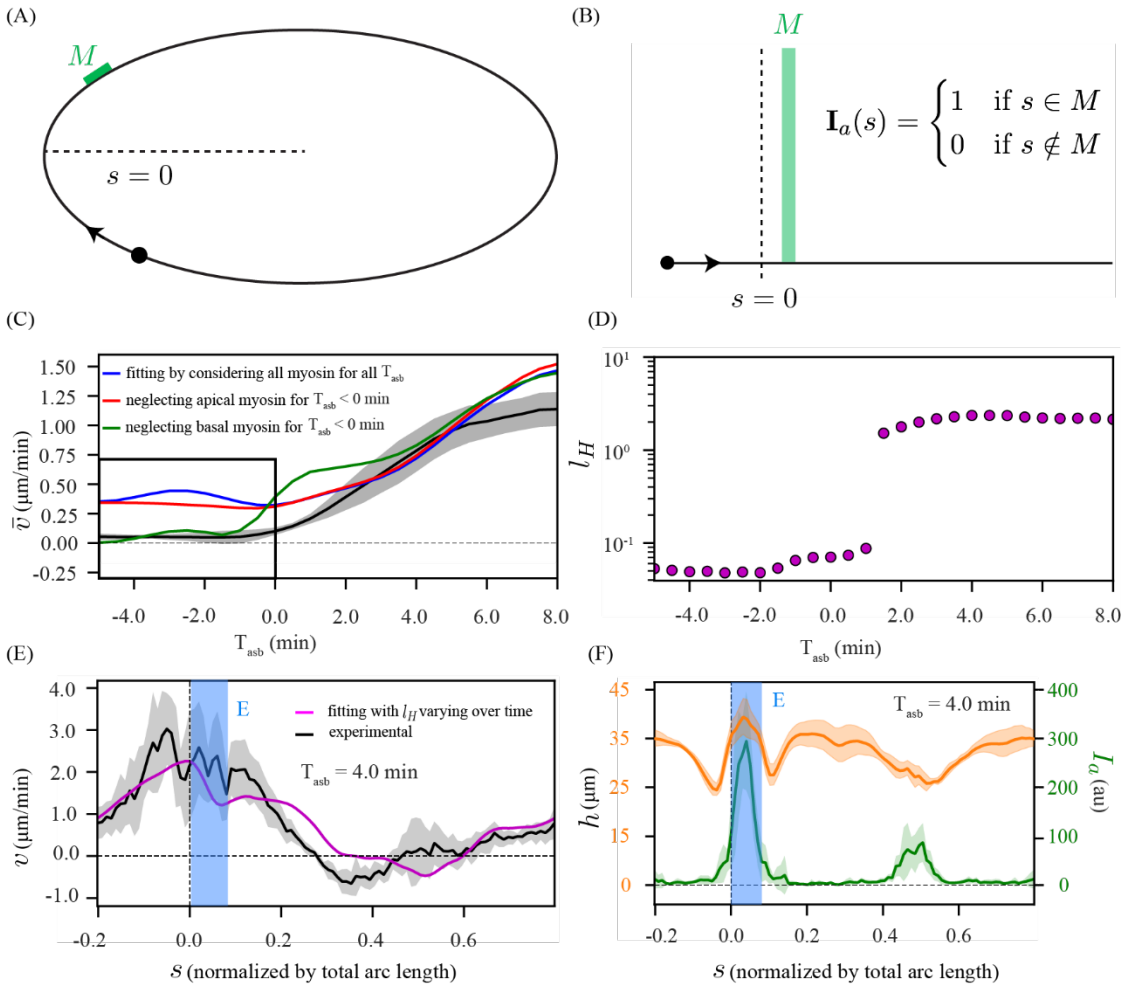

Fig. S6. Fitting with curvature-active moment coupling. (A) Schematic of the elliptic representation of the embryo. Green region corresponds to myosin domain (*M*). **(B)** 1D flat representation of **A**, where the domain M is mathematically described by a rectangular function. **(C)** Experimentally measured temporal profile of spatially averaged velocity $\bar{v}$ (black) and result of three fits (using procedure described in **Fig. 3** in the main text) of equation (3): (1) considering both apical and basal myosin for the entire time range T_{asb} > -5 min (blue), (2) neglecting apical myosin for T_{asb} < 0 min (red) and (3) neglecting basal myosin for T_{asb} < 0 min (green). In fitting all parameters were constan over timet. **(D)** Temporal profile of the hydrodynamic length (l_H) corresponding to the magenta curves in **Fig. 5G, H** in main text. In this plot l_H is given in units of epithelial length L=1000 μm. **(E)** Experimentally measured spatial profile of velocity v (black) and the associated fit curve shown in **Fig. 5H** (magenta, in main text). **(F)** Experimentally measured spatial profile

of the epithelial height (h, orange) and apical myosin intensity (I_a, green) at the same time point as in **E**. The shaded regions associated to experimental data is the standard deviation, computed over 6 embryos.

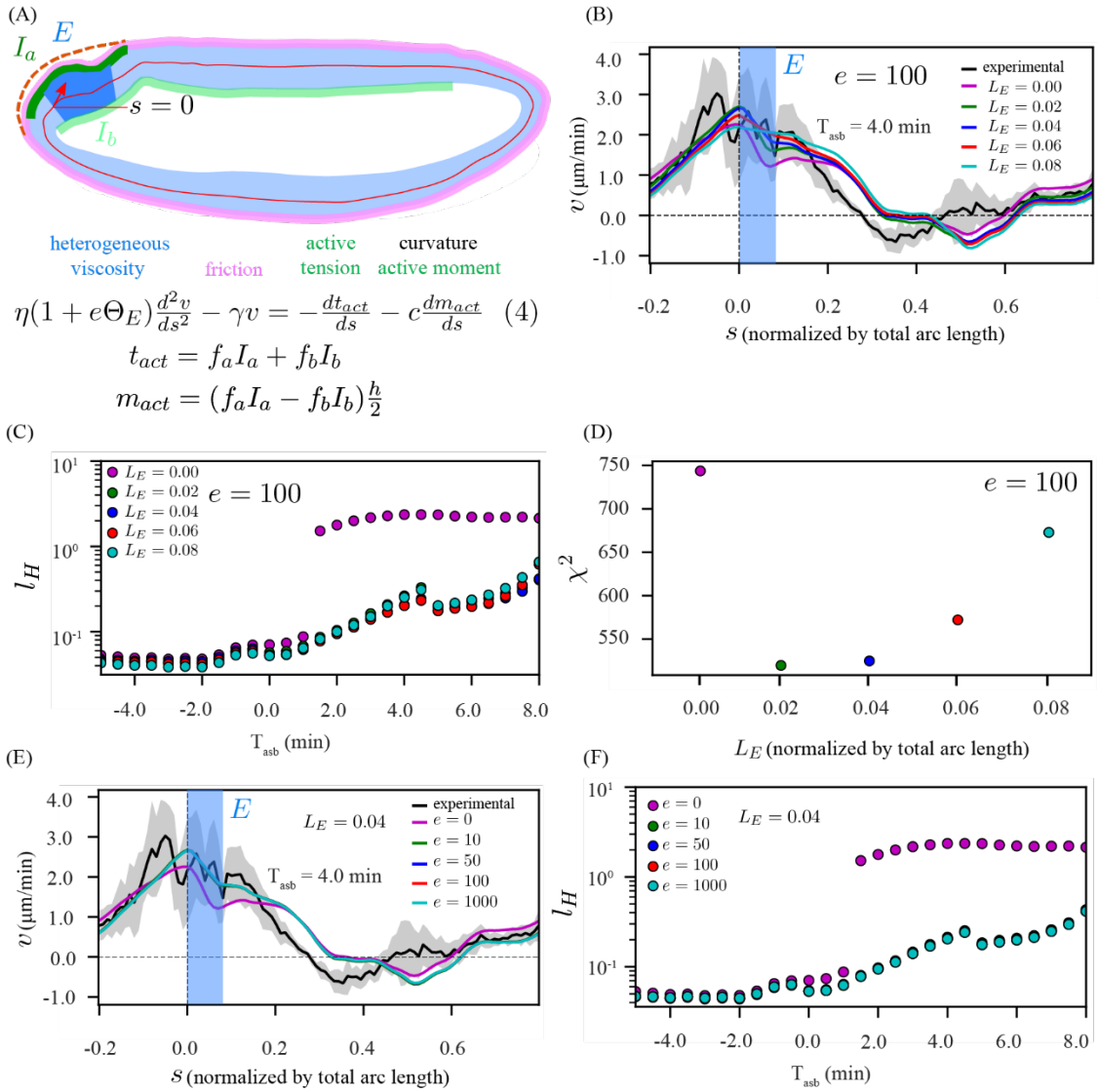

Fig. S7. Curvature-active moment-based model with limited tissue contraction at the region of apical myosin. (A) Schematic representation of our model, equation (4), which is similar to **Fig. 5D** in main text**,** but with an additional domain *E* (dark blue region) where the localized viscosity is increased by a factor *e*. **(B)** Experimentally measured spatial profile of velocity v (black) and result of fits (using procedure described in **Fig. 3** in the main text) of equation (4) with increased value of viscosity fixed at *e* = 100, shown for five values of the length of high viscosity domain L_E (centered around and restricted within the apical myosin domain, and). In fitting, all parameters but the hydrodynamic length (l_H) constant over time. **(C)** Temporal profile of l_H corresponding to fitting described in **B**. **(D)** Comparison of the fit quality for fitting curves in **B**:

chi-square values (χ^2), summed over all time points. **(E)** Similar to panel **B** but fitting was done with a fixed value of the length L_E = 0.04 and for five different values of increase in viscosity *e*. **(F)** Temporal profile of l_H corresponding to fitting described in panel **E**. Here, l_H is given in units of epithelial length L~1000 μm. The shaded regions associated to experimental data is the standard deviation, computed over 6 embryos.

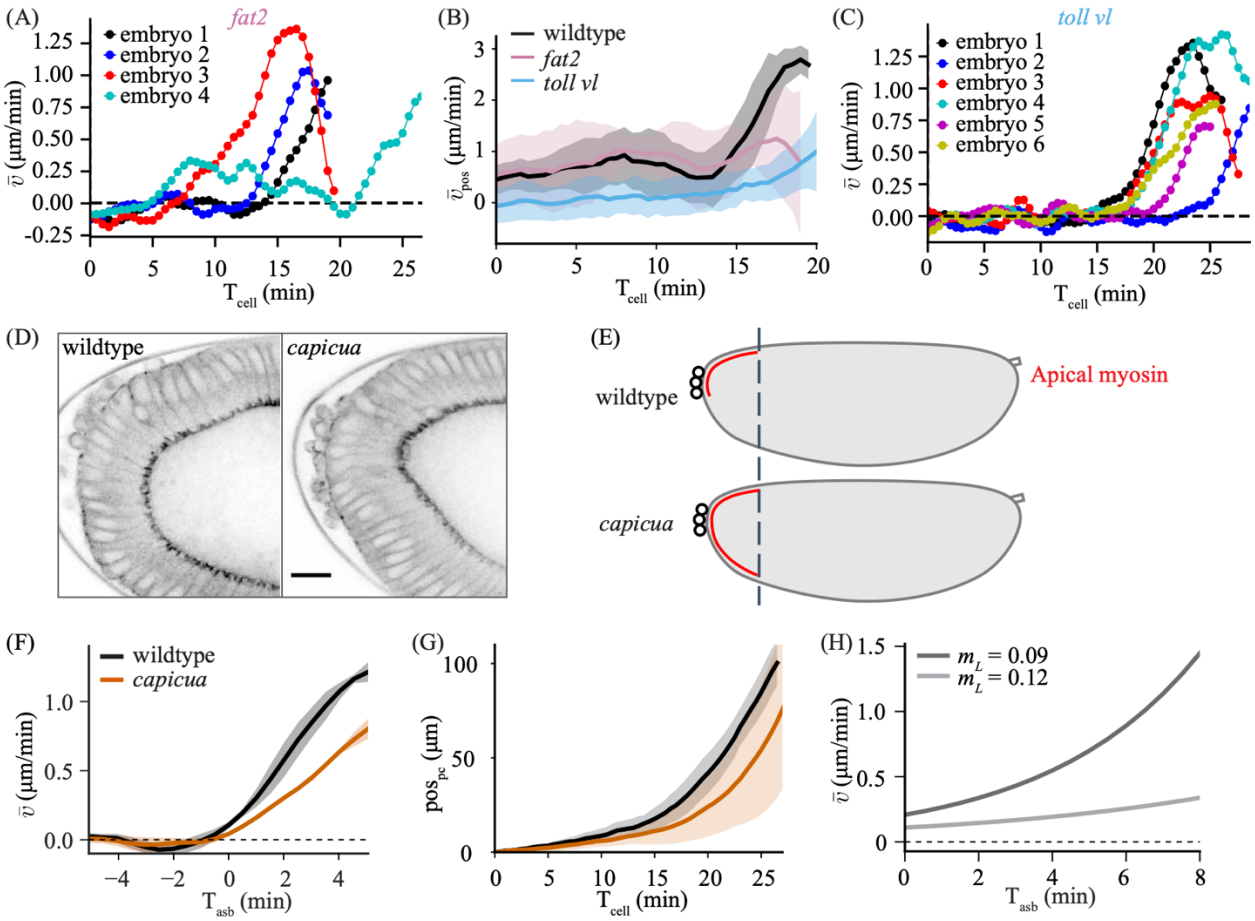

Fig. S8. *fat2* and *capicua* characterization. (A) Temporal profile of $\underline{v}$ for individual *fat2* embryos. **(B)** Temporal profile of posterior averaged velocity $\bar{v}_{pos}$ for wildtype (black), *fat2* (pink), and *toll vl* (blue) embryos. **(C)** Temporal profile of $\bar{v}$ for individual *toll vl* embryos. **(D)** View of the posterior of a wildtype (left) and *capicua* (right) embryo imaged for *sqh*::GFP. Scale bar is 20 µm. Note: the *capicua* embryos were imaged with a single copy of s*qh*::GFP and GAP43::mSc. **(E)** Schematic showing the change in apical myosin domain in *capicua* embryos. **(F)** Experimental spatially averaged tangential velocity as a function of time since symmetry breaking for 5 wildtype, and 5 *capicua* embryos. **(G)** Pole cell position (pos_{pc}) as a function of time for 6 wildtype, and 9 *capicua* embryos. **(H)** Average velocity of tissue flow resulting from simulations performed on elliptical embryos with different length of myosin domain (m_L; see ***SI Appendix***).

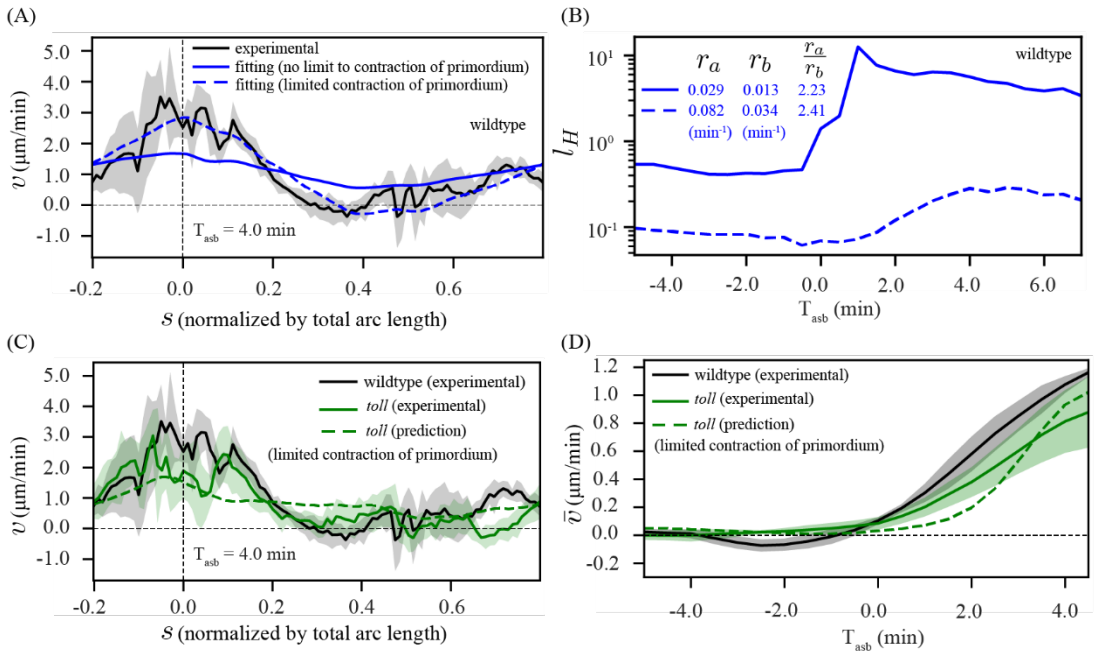

Fig. S9. wildtype, *toll vl*, fitting and prediction. (A) Experimentally measured spatial profile of velocity v (black) in wildtype embryos and result of fits of equation (3) in panel **Fig. 5D** in main text (blue solid curve, no limit to contraction of the primordium) and equation (4) in panel **Fig. S7A** (blue dashed curve, limited contraction of the primordium with e = 100 and L_E = 0.04), representative time T_{asb} = 4 min. The fits were performed using the same procedure as described in **Fig. 5G** (magenta curve in main text). **(B)** Parameters corresponding to fits in panel **A**, temporal profile of the hydrodynamic length l_H (as curves) and other constant parameters r_a, r_b and their ratio (in legend). **(C, D)** Prediction of velocity for *toll vl* using parameters from wildtype in panel **B** (blue dashed line), and myosin and curvature data from *toll vl*. **(C)** Experimentally measured spatial profile of velocity v in wildtype (black) and *toll vl* (green solid curve), and predicted spatial velocity profile for *toll vl* (green dashed curve). **(D)** Experimentally measured temporal profile of spatially averaged velocity $\bar{v}$ in wildtype (black) and *toll vl* (green solid curve), and predicted temporal profile of spatially averaged velocity for *toll vl* (green dashed curve).

Legends for Movies S1 to S8:

Movie S1 (separate file): Time-lapse of early *Drosophila* morphogenesis in a wildtype embryo. Imaged in the sagittal plane on a two-photon microscope labeled with GAP43:mScarlet (top) and *sqh*:GFP (bottom).

Movie S2 (separate file): Tissue dynamics in wildtype and *ets* embryos. Time-lapse of myosin activation in a wildtype (top) and *eve, twist, snail embryo* (bottom) synchronized with respect to the time when the cellularization front passes the nuclei in the dorsal posterior.

Movie S3 (separate file): Tracking of pole cells in a wildtype embryo. Time-lapse of tissue dynamics in an embryo labeled for cell membrane maker GAP43:mScarlet. The green dot shows the position used to calculate pole cell movement over time (as in **Fig. 1D**).

Movie S4 (separate file): Direction of flow in *toll vl* embryos. Time-lapse of three *toll vl* mutant embryos that flow indifferent directions. The top embryo flows dorsally, the middle embryo flows laterally, and the bottom embryo flows ventrally.

Movie S5 (separate file): Tissue dynamics in wildtype, *toll vl,* and *cta* embryos. Time-lapse of myosin activation in a wildtype (top), *toll vl* (middle), and *cta* (bottom) embryos synchronized with respect to the time when the cellularization front passes the nuclei in the dorsal posterior.

Movie S6 (separate file): Tissue dynamics in wildtype and *scab* knockout embryos. Time-lapse of myosin activation in a wildtype (top) and *scab* knockout (bottom) embryos synchronized with respect to the time when the cellularization front passes the nuclei in the dorsal posterior.

Movie S7 (separate file): Tissue dynamics in wildtype and *fat2* embryos. Time-lapse of myosin activation in a wildtype (top) and *fat2* (bottom) embryos synchronized with respect to the time when the cellularization front passes the nuclei in the dorsal posterior.

Movie S8 (separate file): Tissue dynamics in wildtype and *cic* embryos. Time-lapse of myosin activation in a wildtype (top), and *cic* (bottom) embryos synchronized with respect to the time when the cellularization front passes the nuclei in the dorsal posterior.

SI References

1. G. Salbreux, F. Jülicher, Mechanics of active surfaces. *Phys Rev E* **96**, 032404 (2017).

2. K. Bambardekar, R. Clément, O. Blanc, C. Chardès, P.-F. Lenne, Direct laser manipulation reveals the mechanics of cell contacts in vivo. *Proc Natl Acad Sci U S A* **112**, 1416–1421 (2015).

3. A. D'Angelo, K. Dierkes, C. Carolis, G. Salbreux, J. Solon, In vivo force application reveals a fast tissue softening and external friction increase during early embryogenesis. *Curr Biol* **29**, 1564-1571.e6 (2019).

4. A. D. Wessel, M. Gumalla, J. Grosshans, C. F. Schmidt, The mechanical properties of early *Drosophila* embryos measured by high-speed video microrheology. *Biophys J* **108**, 1899–1907 (2015).